Simulating ultracold matter: horizons and slow light

Conor Farrell

PhD

School of Physics and Astronomy,

University of St Andrews

December 7, 2007

Abstract

This thesis explores the links between different ways of modelling the physical world. Finite difference numerical simulations may be used to encode the behaviour of physical systems, allowing us to gain insight into their workings and even to predict their behaviour. Similarly, one can investigate the properties of gravitational black holes through the use of analogue black holes, physical systems which share at least some part of the physics of the astronomical objects. Concentrating on black hole analogues using Bose-Einstein condensates, I show how simulations of these systems may be greatly assisted through the use of a proper absorbing boundary condition, the Perfectly Matched Layer. Such a boundary condition allows the efficient truncation of the computational domain, both saving computational time and increasing accuracy. I then apply this technique to the simulation of the supersonic flow of a Bose-Einstein condensate through a Laval nozzle, a black hole analogue, showing that such a flow should be stable and observable in the laboratory. Moving to a related system, I investigate the optical analogue of the Iordanskii force - the friction resulting from interaction between excitations in a superfluid's normal component and a superfluid vortex - through the simulation of such a vortex in a Bose-Einstein condensate illuminated by slow light, which is light whose group velocity is on the order of metres per second. The interaction of the slow light with the vortex should produce a momentum transfer due to the optical Aharonov-Bohm effect, exerting a force on the vortex. The coupled system of equations describing the condensate-slow light system is simulated, giving some surprising results.

Contents

Introduction **6**

1 Modelling Reality I: Numerical methods **8**

1.1 Finite Difference Methods 12

1.2 Accuracy and Stability 14

1.2.1 Explicit FDM 16

1.2.2 von Neumann stability analysis 16

1.2.3 Implicit FDM 17

1.2.4 The Crank-Nicolson Scheme 18

2 Modelling Reality II: Black hole analogues **20**

2.1 Hawking radiation 24

3 Bose-Einstein Condensation **31**

3.1 What is a Bose-Einstein Condensate? 31

3.1.1 Bose-Einstein condensate production 32

3.2 The Gross-Pitaevskii equation 33

3.3 Bose-Einstein condensate applications 35

4 Slow light **39**

4.1 Electromagnetically Induced Transparency 40

4.2 Dark state dynamics 46

5 The Perfectly Matched Layer and its use **50**

5.1 The Perfectly Matched Layer 50

5.2 Numerical implementation of the GPE with PML terms 53

5.2.1 The Thomas algorithm 56

5.2.2 Extension to 2+1 Dimensions 57

5.2.3 The 2D PML 59

5.2.4 Attractive interaction: Travelling soliton 59

5.2.5 Repulsive interaction: Free expansion of a BEC 61

6 One-dimensional supersonic flow of a quantum gas **63**

6.1 One-dimensional gas flow 64

6.2 Supersonic flow 66

6.3 Horizons 68

6.4 Critical potential 69

6.5 Hawking temperature 71

6.6 Numerical simulation of a 1D supersonic flow 73

7 The optical analogue of the Iordanskii force **77**

7.1 Theoretical background 77

7.1.1 Slow light in a moving BEC 77

7.1.2 The Aharonov-Bohm effect 80

7.1.3 Aharonov-Bohm generated vortex motion 82

7.2 Numerical implementation 86

7.2.1 Methodology 89

7.3 Results 96

Conclusions **101**

References **102**

Declarations

I, Conor Farrell, hereby certify that this thesis, which is approximately 24,000 words in length, has been written by me, that it is the record of work carried out by me and that it has not been submitted in any previous application for a higher degree.

Date: December 7, 2007. Signature of candidate:

I was admitted as a research student in September, 2002 and as a candidate for the degree of Doctor of Philosophy in September, 2002; the higher study for which this is a record was carried out in the University of St Andrews between 2002 and 2007.

Date: December 7, 2007. Signature of candidate:

I hereby certify that the candidate has fulfilled the conditions of the Resolution and Regulations appropriate for the degree of Doctor of Philosophy in the University of St Andrews and that the candidate is qualified to submit this thesis in application for that degree.

Date: December 7, 2007. Signature of supervisor:

In submitting this thesis to the University of St Andrews I understand that I am giving permission for it to be made available for use in accordance with the regulations of the University Library for the time being in force, subject to any copyright vested in the work not being affected thereby. I also understand that the title and abstract will be published, and that a copy of the work may be made and supplied to any bona fide library or research worker, that my thesis will be electronically accessible for personal or research use, and that the library has the right to migrate my thesis into new electronic forms as required to ensure continued access to the thesis. I have obtained any third-party copyright permissions that may be required in order to allow such access and migration.

Date: December 7, 2007. Signature of candidate:

Acknowledgements

I would like to thank my family for supporting me during my time in St Andrews and listening to my many tales of woe as programs repeatedly refused to behave themselves! Thanks also to my supervisor, Professor Ulf Leonhardt, for his advice and help over the years. To all my friends around the world, thanks for keeping me relatively sane during this process! I would also like to thank Dr Stefano Giovanazzi, Dr Tom Philbin, Dr Patrik Öhberg, Dr Tamas Kiss and Dr Julian Henn for discussions and advice. Special thanks to Dr Aly Gillies for fixing my PC on multiple occasions, including right before submission of this thesis! Funding for this degree has been provided through EPSRC, the Leverhulme Trust and the Nicol Trust, for which I am grateful.

Introduction

In this thesis, I will draw parallels between different ways of modelling reality. In Chapter 1, we will discuss the theory behind the creation of numerical simulations of physical systems, concentrating on finite difference simulations. Although numerical simulation is a useful and powerful technique, it has issues that one must be aware of, which we will also discuss. In Chapter 2, we will move on to a different way of modelling reality, the use of analogue models to probe gravitational black holes. Many important elements of the physics of these astronomical objects are mirrored in their analogues, such as the supersonic flow of a Bose-Einstein condensate. Chapter 3 deals with Bose-Einstein condensates in further detail, discussing their history, creation and how their dynamics may be described through the use of the Gross-Pitaevskii equation. Chapter 4 deals with slow light, light whose group velocity is slowed to the order of metres per second. Electromagnetically Induced Transparency, one of the techniques by which this may be achieved, is investigated. Chapter 5 discusses the application of absorbing boundary conditions to numerical simulations, which truncate the domain, allowing greater computational efficiency and reduced error. In particular I consider the Perfectly Matched Layer and its application to nonlinear and matter wave systems. In Chapter 6, the Perfectly Matched Layer is applied to the numerical simulation of a black hole analogue, the supersonic flow of a Bose-Einstein condensate in a Laval nozzle. Further details of the numerical implementation of such simulations are also discussed. Chapter 7 combines elements from all the previous chapters to discuss another simulation,

the optical analogue of the Iordanskii force, which results from friction between the normal and superfluid components of a BEC and is investigated by illuminating a condensate vortex with slow light. The simulation is greatly more intricate than the previous chapter's, involving two coupled partial differential equations in 2+1 dimensions. The techniques needed to deal with such a simulation and its unexpected results are discussed.

Chapter 1

Modelling Reality I:

Numerical methods

We are fortunate in that the world around us is frequently amenable to accurate description by mathematical equations. The rotation of the earth around the sun, the flow of water through a river's banks, the fall of a raindrop; all of these and more can be rendered in the language of mathematics. Models of reality are not limited to mere reproduction of known effects, however, for they can also be used both to predict previously unknown phenomena and to extrapolate future trends from present occurrences, as we can see on the weather report each day.

Many of these models are not easily solved by hand, since derivative terms frequently occur. Methods of dealing with derivatives existed as long ago as the mid-18th century, when Euler [1] employed a simple technique, which has come to bear his name, in the solution of the problem

$$\frac{dx}{dt} = f(x,t), \quad x(0) = a. \tag{1.1}$$

Euler replaced dx/dt by the finite difference approximation $(x_n - x_{n-1})/\Delta t$, leading

to the recurrence relation

$$x_0 = a, \quad x_n = x_{n-1} + \Delta t f(x_{n-1}, t_{n-1}) \tag{1.2}$$

Such a technique, involving the use of well-defined instructions to accomplish a task, is known as an algorithm, after the Persian mathematician al-Khwarizmi. Other algorithms which predate modern computational methods include the Newton-Raphson method, Gaussian elimination and the Lagrange interpolation polynomial.

In order to execute such algorithms, numerical tables containing lists of the values of functions were employed by a human 'computer'. Mechanical calculators, such as Charles Babbage's famous difference engine, were also used, which in turn lead to the birth of the electronic computer in the 1940s as a result of World War II. The increased speed and accuracy of electronic computers made them well suited to problems of numerical analysis and allowed the consideration of increasingly more complicated problems.

Physical phenomena normally fall into one of three classes of problems: equilibrium problems, eigenvalue problems and propagation problems.

Equilibrium problems are those where the steady state endpoint, Γ, of a system is to be determined, subject to boundary conditions; the differential equation

$$D[\Gamma] = a \tag{1.3}$$

is solved in some domain, with boundary conditions

$$B_i[\Gamma] = b_i \tag{1.4}$$

holding on the boundary. Temperature distribution is an example of an equilibrium problem.

Eigenvalue problems are similar, but also require that the value of at least one constant, ϵ, be found with its corresponding function Γ, as in

$$D[\Gamma] = \epsilon E[\Gamma] \tag{1.5}$$

which must be satisfied within some domain, subject to boundary conditions

$$B_i[\Gamma] = \epsilon C_i[\Gamma]. \tag{1.6}$$

Stability analysis of a bridge falls into the category of eigenvalue problems.

Propagation problems, also known as initial boundary value problems, will be the problem class most considered in this thesis. We propagate the solution of the differential equation

$$D[\Gamma] = a \tag{1.7}$$

to determine its subsequent behaviour, given its initial state

$$I_i[\Gamma] = h_i \tag{1.8}$$

and boundary conditions

$$B_i[\Gamma] = b_i, \tag{1.9}$$

although the domain itself is open in one dimension, normally time. Following Richardson's example [2], we can describe propagation problems as marching problems, since the solution is marched forward in time from an initial state in conjunction with the boundary conditions. In general during this thesis, we will be dealing with Dirichlet boundary conditions, which specify the value of the solution at the boundaries as a function of time, though other sorts of boundary conditions exist, such as Neumann boundary conditions, which specify the gradient of the solution at the boundaries.

Partial differential equations (PDEs) can be classified according to the type of curve along which their information propagates. PDEs describing propagation problems are of parabolic or hyperbolic type. Given the second-order PDE

$$Au_{xx} + 2Bu_{xy} + Cu_{yy} + Du_x + Eu_y + F = 0, \tag{1.10}$$

the system it describes can be classified as elliptic, parabolic or hyperbolic depending on the value of the associated matrix

$$\det \begin{pmatrix} A & B \\ B & C \end{pmatrix}. \tag{1.11}$$

If the value of the determinant is greater than 0, the equation is elliptic; if equal to 0, it is parabolic and if less than 0, the equation is hyperbolic.

There are a number of different approaches that can be taken in the numerical simulation of physical effects. Euler's method was an early use of finite difference methods (FDM), where derivative operators in the equations being considered are represented by finite differences. For the simulations in this thesis, FDM were employed due to their simplicity and the regularity of the computational meshes being used, and accordingly they will be discussed at greater length.

Finite element methods (FEM) involve dividing the computational domain with imaginary lines into subdomains, interconnected by nodes. The values of the function at the nodal points are the basic unknown parameters. The combination of the solutions of these subdomains, when we ensure continuity at the nodes, gives the behaviour of the complete domain.

Finite volume methods (FVM) are similar to FEM in that they involve the use of a meshed geometry, with values calculated at discrete sites. The domain in question is divided into control volumes by control surfaces; equations are evaluated for the control volume and differential terms are evaluated at the control surfaces,

diffusion fluxes being conserved through these surfaces. A structured mesh is not required for FVM, which makes them the natural choice for problems with coarse, nonuniform meshes or where the mesh is moved to follow shocks.

Spectral methods are an alternative method of representing derivatives. The function being investigated is approximated by a finite series; depending on whether it is periodic or not, Fourier series or Chebyshev expansions are used. The resulting finite series approximation is then differentiated. As they use global representations of functions, as opposed to the local representations used in FDM *et al*, they tend to be accurate. Normally the Fast Fourier Transform (FFT) is used, as in general only a finite frequency window need be considered. Spectral methods tend to be best suited to smooth problems, as they converge rapidly under such conditions. Conversely, they are unsuitable for problems involving shocks or other discontinuities.

1.1 Finite Difference Methods

As we have seen, the concept behind finite difference representation is very simple; we attempt to solve continuous systems by translating them into discrete systems which capture the nature of the problem and are amenable to computer solution. Fundamentally, FDM involve approximation, as we replace continuous domains by a mesh of discrete points. The solutions obtained are tied to these points and require interpolation techniques to find intervening values. Choosing the correct approximation for difference operators is essential for a successful implementation of FDM.

To illustrate this, let us apply FDM to the simple boundary value problem

$$Lu = f, \quad u = u(x). \tag{1.12}$$

Expanding $u(x + \Delta x)$ in a Taylor series about x, we obtain

$$u(x + \Delta x) = u(x) + \Delta x \frac{\partial u}{\partial x}(x) + O(\Delta x^2). \tag{1.13}$$

$O(\Delta x^2)$ here is Bachmann and Landau's asymptotic O notation [3] which suppresses higher-order terms, instead stating that a term exists whose absolute value is a constant multiple of the absolute value indicated.

Dividing by Δx, we obtain

$$\frac{\partial u(x)}{\partial x} = \frac{u(x + \Delta x) - u(x)}{\Delta x} + \mathrm{O}(\Delta x), \tag{1.14}$$

Employing subscripts, we can write this as

$$\frac{\partial u}{\partial x}_i \approx \frac{u_{i+1} - u_i}{\Delta x}, \tag{1.15}$$

which is the simple forward difference approximation for $\partial u/\partial x$. We say this approximation is first-order in Δx since, if $a(x)$ is the approximation, $|u - a| = O(\Delta x^1)$ as $\Delta x \to 0$.

Similarly, if we expand $u(x - \Delta x)$ in a Taylor series, we get

$$u(x - \Delta x) = u(x) - \Delta x \frac{\partial u}{\partial x}(x) + O(\Delta x^2). \tag{1.16}$$

which gives us the first-order backwards difference approximation

$$\frac{\partial u}{\partial x}_i \approx \frac{u_i - u_{i-1}}{\Delta x}. \tag{1.17}$$

Higher-order accuracy is often more desirable, however. We can construct the second-order central difference equation by subtracting (1.16) from (1.13), as in

$$u(x + \Delta x) - u(x - \Delta x) = 2\Delta x \frac{\partial u}{\partial x}(x) + O(\Delta x^3), \tag{1.18}$$

giving us

$$\frac{\partial u}{\partial x}_i = \frac{u_{i+1} - u_{i-1}}{2\Delta x} + \mathrm{O}(\Delta x^2). \tag{1.19}$$

The central difference formulation has second order truncation error, while both the forward and backward differences are first order. Higher-order approximations are constructed in a similar fashion.

d^2u/dx^2 can be discretized as

$$\begin{aligned}
\frac{d^2u}{dx^2} = \frac{d}{dx}\left(\frac{du}{dx}\right) &\approx \frac{1}{\Delta x}\left[\left(\frac{du}{dx}\right)_{i+1} - \left(\frac{du}{dx}\right)_i\right] \\
&= \frac{1}{\Delta x}\left(\frac{u_{i+1} - u_i}{\Delta x} - \frac{u_i - u_{i-1}}{\Delta x}\right) \\
&= \frac{u_{i+1} - 2u_i + u_{i-1}}{\Delta x^2} + \mathrm{O}(\Delta x^2)
\end{aligned} \tag{1.20}$$

The Laplacian operator in two dimensions is discretized similarly, as

$$\begin{aligned}
\nabla &= \frac{\partial^2 u}{\partial x^2} + \frac{\partial^2 u}{\partial y^2} \\
&= \frac{u_{i+1,j} - 2u_{i,j} + u_{i+1,j}}{\Delta x^2} + \frac{u_{i,j+1} - 2u_{i,j} + u_{i,j+1}}{\Delta y^2} + \mathrm{O}(\Delta x^2, \Delta y^2)
\end{aligned} \tag{1.21}$$

We now have the basic tools we will need in order to model the real world. However, to ensure the simulation corresponds to reality, we need to take some more subtle matters into consideration, as we shall see.

1.2 Accuracy and Stability

The two primary sources of error in any computer simulation (barring of course human error in coding it!) are truncation error and roundoff error. Truncation error arises from the representation of continuous objects in discrete terms, as we have already seen in the derivation of the finite difference forms of du/dx and d^2u/dx^2. The choice of finite difference representation is vital for the correct

functioning of the program; one must choose a method which gives an error that will not appreciably distort the results, but which also allows the program to run in a realistic timescale.

Roundoff error is a consequence of the limitations of computer hardware. Numbers are stored in memory as patterns of bits, either as fixed point (integer) or floating point (real) numbers. Integer arithmetic is exact, but real arithmetic is prone to small errors in the least significant bits. They are represented in the form

$$\text{Sign} \times \text{Base}^{\text{Exponent}-\text{Bias}} \times \text{Mantissa}$$

where the mantissa and exponents are integers, the base is normally 2 and the bias is a machine-dependent constant integer. Mantissas are generally represented in normalized form, that is to say, the significant bits are shifted as far to the left as possible by being multiplied by the base, the rest of the bit string being zeros, and the exponent being reduced correspondingly. Adding two real numbers, then, is performed by right-shifting the mantissa of the number of lesser magnitude and correspondingly increasing its exponent until it equals the larger number's; if the magnitudes differ too much, the mantissa will be right-shifted to zero, producing the strange result that the addition of a finite number gives no change. Obviously this is far from ideal, but there is little that can be done by the programmer about this aspect of machine architecture except to be aware of the smallest number which produces a result different from 1.0 when added to it, termed the machine accuracy, and to ensure that the problem is scaled accordingly. Essentially, any floating point arithmetic operation will give roundoff error of the magnitude of the machine accuracy, which will accumulate over the course of the program running. Subtracting two numbers that are very nearly equal increases the problem, since the answer will contain only the low-order bits representing the small difference. Such operations can cause the roundoff error to grow to present a serious problem.

Beyond choosing between forward, backward and central differences of various orders of truncation error, we must also choose how an initial value problem marches on in time. The available strategies can be broadly divided into explicit and implicit schemes. As the parabolic Gross-Pitaevskii equation is central to this thesis, we will consider these schemes as applied to the simple diffusion equation

$$\frac{\partial u}{\partial t} - \alpha \frac{\partial^2 u}{\partial x^2} = 0, \, \alpha > 0. \tag{1.22}$$

1.2.1 Explicit FDM

A basic explicit scheme for the diffusion equation is

$$\frac{u_n^{t+1} - u_n^t}{\Delta t} = \frac{\alpha(u_{n+1}^t - 2u_n^t + u_{n-1}^t)}{\Delta x^2} + \mathrm{O}(\Delta t, \Delta x^2). \tag{1.23}$$

We call this scheme explicit since we can directly calculate u_n^{t+1} from known quantities at the current time step. As we use the forward difference for time and a central difference for space, this method is known as the forward-time centred-space (FTCS) method. More sophisticated explicit methods also exist, such as the Dufort-Frankel and leapfrog methods.

1.2.2 von Neumann stability analysis

However, explicit schemes may be unstable, which causes any roundoff error that may be present in the initial solution to be magnified, eventually swamping the system with an incorrect solution. One of the most common methods of investigating stability is von Neumann stability analysis. We assume that the coefficients of the difference equation can be considered constant in space and time over the space and time scales being used. This suggests solutions of the form

$$u_n^t = \xi(k)^t \exp(ikn\Delta x), \tag{1.24}$$

where k is a wavenumber and $\xi(k)$ is a term known as the amplification factor for mode k. Clearly, if $|\xi(k)| > 1$ for any mode, that mode will grow exponentially and swamp the system. Substituting (1.24) into (1.23), we get

$$\xi(k) = 1 - \frac{4\alpha\Delta t}{\Delta x^2} \sin^2\left(\frac{k\Delta x}{2}\right) \tag{1.25}$$

which implies that, for the scheme to be stable,

$$\frac{2\alpha\Delta t}{\Delta x^2} \leq 1. \tag{1.26}$$

For equations nonlinear in u, von Neumann analysis linearizes by writing $u = u_0 + \delta u$ and expanding to linear order in δu. The u_0 terms are assumed to satisfy the difference equation exactly and we then look for unstable solutions around δu. von Neumann analysis, while not to be relied on absolutely, is simple to apply and, in general, gives a good indication of whether or not a particular scheme will be stable. There are alternate methods of stability analysis, such as matrix stability analysis, which can be used to consider the effects of boundary conditions of the problem, something that von Neumann analysis does not take into account.

In the FTCS case, the timestep can be no larger than the time taken to diffuse across a distance Δx. This constraint linking the space and time steps may prove inconvenient in modelling real problems, as features of interest are generally on a scale much greater than Δx; in consequence, many timesteps must be performed. To sidestep this restriction, we can turn to implicit schemes.

1.2.3 Implicit FDM

Implicit schemes, in contrast, have multiple terms at timestep $t + 1$:

$$\frac{u_i^{t+1} - u_i^t}{\Delta t} = \frac{\alpha(u_{i+1}^{t+1} - 2u_i^{t+1} + u_{i-1}^{t+1})}{\Delta x^2} \tag{1.27}$$

Implicit schemes have the advantage of being unconditionally stable; the amplification factor for this equation, as obtained via von Neumann stability analysis, is

$$\xi = \frac{1}{1 + \frac{4\alpha\Delta t}{\Delta x^2}\sin^2\left(\frac{k\Delta x}{2}\right)} \tag{1.28}$$

and so $|\xi| < 1$ for any Δt, which means that the scheme will converge to the correct equilibrium solution regardless of the timestep size, though the intermediate evolution may be inaccurate. Unfortunately, this method is only first-order accurate in time; furthermore, it requires the calculation of a matrix inversion, which can be a computationally intensive task unless the matrix is sparse (as it fortunately is in this case). Simple implicit methods are also not well suited for multidimensional problems, as very large matrices must be manipulated.

1.2.4 The Crank-Nicolson Scheme

A middle way is the use of the Crank-Nicolson scheme, which takes the average of the implicit and explicit schemes. While still requiring a matrix inversion, this has the advantage over fully implicit schemes in that it is second-order accurate in time, although small-scale features of the problem are not done away with as in the fully implicit case. The diffusion equation becomes

$$\frac{u_i^{t+1} - u_i^t}{\Delta t} = \frac{\alpha}{2\Delta x^2}\left((u_{i+1}^{t+1} - 2u_i^{t+1} + u_{i-1}^{t+1}) + (u_{i+1}^t - 2u_i^t + u_{i-1}^t)\right). \tag{1.29}$$

Both sides of the equation are centred at timestep $t + 1/2$ and it is thus second-order in time, while clearly being second-order in space also.

Using von Neumann analysis, we find that the amplification factor is

$$\xi = \frac{1 - \frac{2\alpha\Delta t}{\Delta x^2}\sin^2\left(\frac{k\Delta x}{2}\right)}{1 + \frac{2\alpha\Delta t}{\Delta x^2}\sin^2\left(\frac{k\Delta x}{2}\right)} \tag{1.30}$$

and the equation is stable for any choice of timestep. All of the above methods

are specific cases of the more general formulation

$$\frac{u_i^{t+1} - u_i^t}{\Delta t} = \alpha \frac{\theta(u_{i+1}^{t+1} - 2u_i^{t+1} + u_{i-1}^{t+1}) + (1-\theta)(u_{i+1}^t - 2u_i^t + u_{i-1}^t)}{\Delta x^2}. \tag{1.31}$$

where $0 \leq \theta \leq 1$. von Neumann stability analysis shows that the stability condition is

$$\begin{aligned} \frac{2\alpha\Delta t}{\Delta x^2} < \frac{1}{1-2\theta} \text{ if } 0 \leq \theta < 1/2, \\ \text{No restriction if } 1/2 \leq \theta \leq 1. \end{aligned} \tag{1.32}$$

Now that we have covered the basics of modelling reality via finite difference, let us turn to a topic on the surface dissimilar, yet fundamentally related - the means by which one studies a black hole.

Chapter 2

Modelling Reality II:

Black hole analogues

Obviously, it is not practical to create a gravitational black hole in your laboratory (not to mention any possible safety concerns!). How then can we investigate the properties of these astronomical objects in a more direct fashion than interpreting data from telescopes? A possible solution is the use of artificial black holes, also known as black hole analogues. A useful analogue black hole should be a physical system that is experimentally feasible and reproduces the underlying physics of gravitational black holes in a meaningful way. As black holes are like space-time rivers, such analogue models often involve flowing fluids.

Consider the fate of the fish in the picture below. If the water's flow speed increases as it approaches the waterfall, but the fish are only able to swim at a maximum speed s, once the speed of the flow exceeds this maximum, fish will be unable to swim back upstream and will inevitably be swept downstream to their doom; we could term the point of no return a fish horizon.

A more sensible black hole analogue is sound in a flowing fluid. Once again, let us assume the fluid velocity increases as we move along the fluid's length. If the fluid velocity through a certain surface exceeds the speed of sound in that fluid,

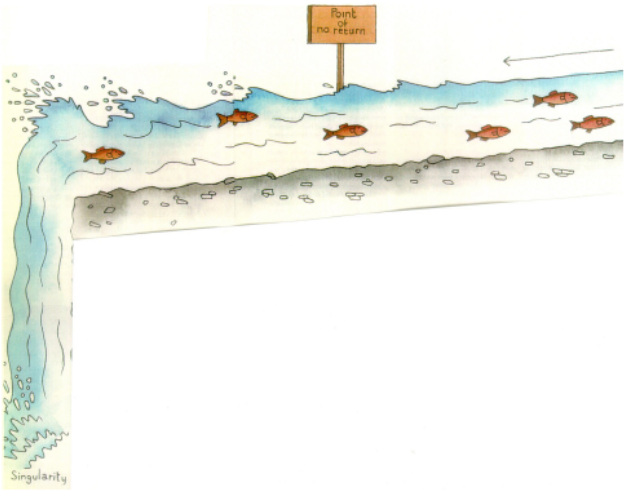

Figure 2.1: A black hole analogue in action

it will become impossible for sound waves in the fluid, similar to the fish in the previous example, to travel back through that surface, called the sonic horizon.

We may ask ourselves whether the resemblance between this case and a gravitational black hole has any real significance. Fortunately, it does [4]. Although spacetime itself is not physically curved in black hole analogues, which differs from the region around a gravitational black hole, small oscillations in analogue systems behave as though they are inhabiting an effectively curved spacetime since they experience focussing or defocussing effects.

Let us consider the irrotational fluid mechanical description of sound waves in the moving medium, assuming it is barotropic so that pressure does not create vortices and further assuming that it is flowing slowly enough that we can treat it in a non-relativistic fashion. For simplicity, also assume the fluid is inviscid. The flow is the gradient of a velocity potential, with curl zero;

$$\mathbf{u} = \nabla\phi \tag{2.1}$$

The dynamical equations governing this system are

$$\frac{\partial \rho}{\partial t} + \nabla \cdot (\rho \mathbf{u}) = 0, \tag{2.2}$$

the continuity equation,

$$\rho \left(\frac{\partial \mathbf{u}}{\partial t} + (\mathbf{u} \cdot \nabla)\mathbf{u} \right) = -\nabla p, \tag{2.3}$$

the Euler equation and

$$p = p(\rho) \tag{2.4}$$

a barotropic equation of state.

Linearizing around some exact solution ρ, ϕ and p consist of a background field plus some small correction:

$$\phi = \phi_0 + \xi\phi_1 + \dots$$

$$\rho = \rho_0 + \xi\rho_1 + \dots$$

$$p = p_0 + \xi p_1 + \dots$$

This leads to the following equations of motion for the linearized fluctuations:

$$\frac{\partial \rho_1}{\partial t} + \nabla \cdot (\rho_1 \nabla\phi_0 + (\rho_0 \nabla\phi_1) = 0, \tag{2.5}$$

$$\rho_0 \left(\frac{\partial \phi_1}{\partial t} + \nabla\phi_0 \cdot \nabla\phi_1 \right) = p_1, \tag{2.6}$$

$$p_1 = c^2_{\text{sound}} \rho_1, \tag{2.7}$$

where $c^2_{\text{sound}} = \partial p / \partial \rho$. This system of equations is equivalent to the second-order

PDE

$$\frac{\partial}{\partial t}\left(c_{\text{sound}}^{-2}\rho_0\left(\frac{\partial\phi_1}{\partial t}+\mathbf{u}_0\cdot\nabla\phi_1\right)\right) = \nabla\cdot\left(\rho_0\nabla\phi_1 - c_{\text{sound}}^{-2}\rho_0\mathbf{u}_0\left(\frac{\partial\phi_1}{\partial t}+\mathbf{u}_0\cdot\nabla\phi_1\right)\right). \tag{2.8}$$

Using the standard notation for four-dimensional coordinates, $x^\mu \equiv (t,\mathbf{x})$, we introduce the 4×4 matrix

$$g^{\mu\nu}(t,\mathbf{x}) = \frac{1}{\rho_0 c_{\text{sound}}}\begin{bmatrix} -1 & -u_0^j \\ -u_0^i & (c_{\text{sound}}^2\delta^{ij} - u_0^i u_0^j)\end{bmatrix}. \tag{2.9}$$

This allows us to transform (2.8) to

$$\frac{1}{\sqrt{-g}}\frac{\partial}{\partial x^\mu}\left(\sqrt{-g}\,g^{\mu\nu}\frac{\partial}{\partial x^\nu}\phi_1\right)=0 \tag{2.10}$$

where $g = 1/(\det(g^{\mu\nu}))$.

This equation is that of a minimally coupled massless scalar field propagating in a spacetime with metric $g_{\mu\nu}$, which describes signal propagation in the curved space;

$$g_{\mu\nu} = \frac{\rho_0}{c_{\text{sound}}}\begin{bmatrix} -(c_{\text{sound}}^2 - u_0^2) & -(u_0)_j \\ -(u_0)_i & \mathbf{I}\end{bmatrix}, \tag{2.11}$$

$\mathbf{I}$ being the unity matrix. In other words, provided the fluid is inviscid and barotropic, the equation describing sound in a fluid is the same as the d'Alembertian equation of motion describing scalar waves in (3+1)-dimensional Lorentzian geometry. It is clear that the behaviour of sound waves in the flowing fluid is analogous to the fate of light in a gravitational black hole. This allows us to investigate kinematic properties of general relativity, in other words, those related to a Lorentzian geometry. As the acoustic metric obeys the rules of fluid mechanics rather than the Einstein equations of general relativity, what we can say about its dynamical

behaviour is somewhat more limited.

As Unruh [4] showed, there is evidence that a thermal spectrum of sound waves should be emitted from such a sonic horizon, the sonic analogue of Hawking radiation [5, 6] emitted from a gravitational black hole. This further implies that the resemblance between flowing fluid and a gravitational black hole is more than merely superficial; it should, in theory, be possible to observe Hawking radiation in the laboratory, using a so-called dumb hole.

2.1 Hawking radiation

Hawking radiation is a kinematical effect which occurs in all Lorentzian geometries in which an event horizon is present and so depends entirely on the effective metric [7]. It means that black holes are not really black, but instead lose energy in the form of thermal radiation, cased by vacuum fluctuations. This is often explained in terms of a particle-antiparticle pair being created from vacuum near the event horizon; normally, they would annihilate one another, but near a black hole one passes the event horizon and becomes trapped, while the other escapes, taking some of the black hole's energy with it. Going back to our waterfall example, let us assume that the speed with which the water flows near the horizon is $\mathbf{u} = -c+\alpha x$. Dimensional analysis tells us that α has the dimensions of time^{-1}. The Hawking temperature is then necessarily proportional to $\hbar\alpha$; as we will see later, it turns out to be [5]

$$kT = \frac{\hbar\alpha}{2\pi} \tag{2.12}$$

To gain a better understanding of the fundamental principles behind Hawking radiation, let us consider a simple system, namely light in a moving medium. Light near the horizon will be compressed to very small wavelengths as it struggles against being swept away. This small length scale dominates the system; effects in the x and y directions are not important and hence we can consider the problem as

a purely $(1+1)$-dimensional one. Let us further assume that the refractive index of the medium $\sqrt{\epsilon}$ is very large, allowing us to use a non-relativistic treatment. Light is described by the Lagrangian density

$$\mathcal{L} = \frac{\epsilon_0}{2}\left(\epsilon E'^2 - c^2 B'^2\right) \tag{2.13}$$

where the primes denote the moving frame;

$$E' = -(\partial_t + \mathbf{u}\partial_z)A,\ B' = \partial_z A, \tag{2.14}$$

A being the vector potential in 1D.

We derive the equation of motion from the Lagrangian in the normal way

$$\frac{\partial \mathcal{L}}{\partial A} = \partial_t \frac{\partial \mathcal{L}}{\partial(\partial_t A)} + \partial_z \frac{\partial \mathcal{L}}{\partial(\partial_z A)}. \tag{2.15}$$

To discuss the Hawking effect, we must consider the quantum fields, which we assume are quantum operators and can be decomposed into modes as

$$\hat{A} = \Sigma_k A_k(z,t)\hat{a}_k + A_k^*(z,t)\hat{a}_k^\dagger. \tag{2.16}$$

Let us define the scalar product of the mode functions

$$(A_k, A_l) = \frac{i\epsilon_0}{\hbar}\int (A_k^*(\partial t + \partial_z \mathbf{u})A_l - A_l(\partial t + \partial_z \mathbf{u})A_k^*)\,\epsilon\,\mathrm{d}z \tag{2.17}$$

This scalar product is invariant under evolution and plays a similar role to standard quantization of the electromagnetic field. If we require that the mode functions are normalized as

$$(A_k, A_l) = \delta_{kl},\ (A_k, A_l^*) = 0 \tag{2.18}$$

then from the Heisenberg commutator, (2.16) and (2.18)

$$[\hat{a}_k, \hat{a}_l^\dagger] = \delta_{kl},\ [\hat{a}_k, \hat{a}_l] = 0. \tag{2.19}$$

We can express the modes $\hat{a}_k, \hat{a}_k^\dagger$ in terms of $\hat{A}$:

$$\hat{a}_k = (A_k, \hat{A}),\ \hat{a}_k^\dagger = -(A_k^*, \hat{A}). \tag{2.20}$$

Waves propagating in the medium can be expressed in the form $A = A_+(t_+) + A_-(t_-)$ as a superposition of counter- and co-propagating plane waves, respectively. We assume ϵ is constant for simplicity. t_+ and t_- are modified coordinates such that

$$t_\pm = t - \int \frac{dz}{\mathbf{u} \pm c}. \tag{2.21}$$

When there is no movement of the fluid we obtain the d'Alembert solution. We will consider waves that propagate against the current, as waves travelling with the current produce no radiation. On the right-hand side of the event horizon, the mode function is

$$A_R = \mathcal{A}_R \Theta(z) \exp(-i\omega t_+) \tag{2.22}$$

and on the left-hand side it is

$$A_L = \mathcal{A}_L \Theta(-z) \exp(i\omega t_+). \tag{2.23}$$

$\Theta(\pm z)$ is a unity step fuction which ensures that A_R exists only on the right side of the horizon and vice versa for A_L. On the left side of the event horizon, we must use the negative frequency $-\omega$ in order to have a mode with positive norm. We can see that

$$i(\partial_t + \mathbf{u}\partial_z)A_L = -\omega \frac{c}{u + c} A_L; \tag{2.24}$$

the flow u and c are negative beyond the horizon, so ω must be as well. A negative

frequency implies a negative energy $-\hbar\omega$. This means that, in the model we are considering with fixed ϵ and u, neglecting the light's action on the medium, the black hole does not have a natural ground state. The Hamiltonian for this system is

$$\hat{H} = \sum_k \hbar\omega_z (A_R^\dagger A_R - A_L^\dagger A_L) \tag{2.25}$$

Mixing various modes and the annihilation and creation operators can result in states of the same energy. This is a similar idea to parametric amplification; we can write

$$\begin{aligned} A_1 &= A_R \cosh\xi + A_L^* \sinh\xi,\ A_2 = A_R^* \sinh\xi + A_L \cosh\xi \\ a_1 &= \hat{a}_R \cosh\xi - \hat{a}_L^\dagger \sinh\xi,\ a_2 = -\hat{a}_R^\dagger \sinh\xi + \hat{a}_L \cosh\xi \end{aligned} \tag{2.26}$$

where ξ is some parameter of the system. These combinations leave the energy of the system invariant. How, then, can we define the vacuum state, the state annihilated by all annihilation operators, when different combinations of operators will produce different vacuum states? We can avoid this conundrum by realising that the vacuum state must depend on the history of how the event horizon was formed. At some point in the past, the fluid was accelerated to greater than the speed of sound. We assume that in the past we can describe the mode functions of the system in terms of smooth wavepackets. We also assume that the process which created the event horizon was relatively smooth. Before the collapse, wavepackets can be separated into analytic wavepackets travelling with or against the flow and these properties continue after the horizon is formed. The functions A_R and A_L are clearly not analytic, due to the step function, so we must take combinations of them which are, which will correspond to the vacuum state.

Near the horizon, which we will take to be at $z = 0$, the speed of the flow is given

by $u \approx -c + \alpha z$, where α is the velocity gradient at the horizon. Here,

$$t_+ \approx t - \frac{\ln(z)}{\alpha} \tag{2.27}$$

so the analytic combinations obtained from the Bogoliubov transformation are

$$\begin{aligned} A_1 &= \mathcal{A}\left(\Theta(z) z^{i\omega/\alpha} \cosh\xi + \Theta(-z)(-z)^{i\omega/\alpha} \sinh\xi\right) \\ A_2 &= \mathcal{A}\left(\Theta(z) z^{-i\omega/\alpha} \sinh\xi + \Theta(-z)(-z)^{-i\omega/\alpha} \cosh\xi\right) \end{aligned} \tag{2.28}$$

We can also see that since

$$(-1)^{i\omega/\alpha} = \exp(\pi\omega/\alpha) \tag{2.29}$$

we can exactly compensate for the $(-z)$ terms by adjusting the cosh and sinh, the correct ratio being

$$\tanh\xi = \exp(-\pi\omega/\alpha), \tag{2.30}$$

which describes a two-mode squeezed vacuum state; $a_1|0\rangle = a_2|0\rangle = 0$. The expectation value of the energy is the part of the Bogoliubov transformation where the equation operators appear squared, *i.e.*

$$\left\langle \hat{a}_R^\dagger \hat{a}_R \right\rangle = \sinh^2\xi = \frac{1}{\exp 2\pi\omega/\alpha - 1}. \tag{2.31}$$

We can also write this as the Planck distribution

$$\frac{1}{\exp(\hbar\omega/kT) - 1}. \tag{2.32}$$

which was Hawking's finding. A similar derivation can be carried out for Bose-Einstein condensates, although this is more complicated as it involves Bogoliubov excitations [8].

Indeed, there is some evidence [9] that the presence of a horizon is not strictly necessary to observe Hawking radiation in black hole analogues, provided the system asymptotically approaches a state containing a horizon sufficiently quickly. This finding could lead to useful laboratory black hole analogues by avoiding the instabilities that supersonic flow in a superfluid, for example, can lead to [10].

Using a black hole analogue, we should be able to gain insight into behaviour at distances less than the Planck length, 1.616×10^{-35}m. At such small distances, quantum indeterminacy dominates and the concept of distance itself breaks down. A true horizon will generate both trans-Planckian physics and Hawking radiation, but the extent to which trans-Planckian effects influence Hawking radiation is currently unclear; the investigation of this question is an important motivator for black hole analogues. In theory we should be able to gain information about these extreme conditions because waves leaving a black hole's event horizon are red-shifted as they travel away from it. This implies that if we could travel backwards in time along with waves travelling inward, we would observe them being blue-shifted to ever-higher energies, eventually becoming on the order of the Planck energy, 1.22×10^{19} GeV, related to the Planck length by the uncertainty principle and either reaching infinity at the event horizon itself or leading to a failure of general relativity [11].

As the typical temperature of Hawking radiation is only 10^{-7}K for a solar-mass gravitational black hole, which is very much less than the temperature of the cosmic microwave background radiation, it proves an extreme experimental challenge to measure directly. In contrast, Hawking radiation temperatures in a transsonic alkali Bose-Einstein condensate, which we will discuss in the next chapter, while only on the order of 15nK, are very much higher than the background temperature of $\sim$ 1nK and so should be much more amenable to detection. BECs also have the advantage over superfluids such as Helium-3 and Helium-4; while the former is a complex quantum liquid ripe with analogies between the behaviour

of its elementary interactions and general relativity [12], such analogies have not yet been directly observed experimentally. Helium-4, due to the Landau criterion [13] will lose superfluidity long before it reaches the speed of sound, making it unsuitable for use in sonic black holes. Understanding the Hawking effect would be an important step on the way to a quantum theory of gravity [14].

Chapter 3

Bose-Einstein Condensation

3.1 What is a Bose-Einstein Condensate?

The foundations of Bose-Einstein statistics - the statistical distribution of identical, indistinguishable particles with integer spin over energy states in thermal equilibrium - were described by the Indian physicist Bose in a 1924 paper [15], where he derived the Planck distribution law for photons through statistical arguments alone; Einstein arranged for it to be published and extended it to cover general, non-photonic cases [16], called bosons. Einstein predicted that at very low temperatures, even non-interacting particles would undergo a phase transition - Bose-Einstein condensation. Also in the early 1920s, in order to help explain the Bohr model of the atom, de Broglie theorized that particles could also possess wave-like properties. The de Broglie wavelength, $\lambda_{\mathrm{dB}} = h/p$, gives the effective wavelength of a particle, the same relationship as that of a photon. At normal temperatures, this wavelength is tiny. Near absolute zero, however, particles move very slowly and so the de Broglie wavelength can have a macroscopic value, dominating the characteristics of the system.

A Bose-Einstein condensate (BEC) occurs because, in the limit of an infinite 3D volume, the total number of energy states as the energy tends to zero becomes

extremely small. This forces multiple atoms to occupy the same state, the lowest energy one available. In the thermodynamic limit, when both the particle number and the volume grow to infinity, the system changes state, undergoing a phase transition.

At such low temperatures, the de Broglie wavelengths of the individual atoms will overlap, producing a kind of 'super-atom' whose behaviour is described by a single quantum mechanical wavefunction. As the system temperature decreases, the phase space density of atoms increases; once there is more than one atom per cell of phase space (a cube of side length λ_{dB}), Bose-Einstein condensation occurs.

3.1.1 Bose-Einstein condensate production

This new state of matter was first created in June 1995 by Cornell and Wieman's group at JILA using rubidium-87 atoms [17], as they could be excited by contemporarily-available lasers and also had a favourable energy-level structure for laser cooling. At about the same time, Ketterle's group at MIT, using sodium atoms, had created a condensate containing approximately two orders of magnitude more atoms [18]. For this work, the three received the Nobel Prize in 2001.

The pioneering condensates were created in the following manner: first, laser cooling was performed on atoms held in a magneto-optical trap. Once the atoms were no longer capable of being cooled by laser light, evaporative cooling was performed in a magnetic trap. This is done by applying a varying radio-frequency field which excites the fast, relatively hot atoms, allowing them to escape, a process known as RF evaporation. The remaining atoms then rethermalise through collisions. Once the temperature falls past the critical value, BEC occurs. For the JILA experiment, the critical temperature was 170 nK and the number density was 2.5×10^{12} per cubic centimetre. That the atoms had truly condensed was verified by switching off the trap and allowing the contents to expand; optical imaging of the time of flight revealed a sharp peak in the velocity distribution below a critical

temperature, strong evidence that BEC had occurred.

Furthermore, the creation of a fermionic condensate of potassium-40 atoms was reported recently [19]. This was achieved through the creation of fermionic pairs, which behave like bosons, by subjecting the atoms to a magnetic field which creates a Feshbach resonance, causing the interaction between them to become highly attractive. Such a fermionic condensate could provide important insight into superfluidity and superconductivity.

3.2 The Gross-Pitaevskii equation

Let us consider how best to describe the behaviour of a BEC. The initial investigation into confined weakly-interacting bosons was carried out in the late 1950s, by Gross and Pitaevskii [20, 21].

In second quantization, the many-body Hamiltonian which describes N interacting particles confined by a potential V_{ext} is

$$\begin{aligned}\hat{H} = &\int d\mathbf{r}\hat{\Psi}^{\dagger}(\mathbf{r})\left[-\frac{\hbar^2}{2m}\nabla^2 + V_{ext}(\mathbf{r})\right]\hat{\Psi}(\mathbf{r}) \\ &+ \frac{1}{2}\int d\mathbf{r}d\mathbf{r}'\hat{\Psi}^{\dagger}(\mathbf{r})\hat{\Psi}^{\dagger}(\mathbf{r}')V(\mathbf{r}-\mathbf{r}')\hat{\Psi}(\mathbf{r}')\hat{\Psi}(\mathbf{r}) \qquad (3.1)\end{aligned}$$

Here $\hat{\Psi}(\mathbf{r})$ and $\hat{\Psi}^{\dagger}(\mathbf{r})$ are bosonic field operators that respectively destroy and create a particle at $(\mathbf{r})$. $V(\mathbf{r}-\mathbf{r}')$ is the two-body interatomic potential; as it is so dilute, s-wave collisions dominate the system. However, this equation may be difficult or impossible to solve in reasonable time for large values of N. The natural alternative is a mean-field equation, which abstracts the effects of the myriads of interactions, replacing them with an average or effective term; this reduces the many-body problem to an effective one-body problem. For time-dependence in the case of BECs, this consists of separating out the condensate contribution to the bosonic field operator $\hat{\Psi}(\mathbf{r},t)$ by dividing it into a classical condensate part,

$\psi(\mathbf{r},t)$, and an excitation term $\hat{\phi}(\mathbf{r},t)$. $\psi(\mathbf{r},t)$ is an order parameter, often called the wave function of the condensate, which is defined as the expectation value of the field $\psi = \left\langle \hat{\Psi}(\mathrm{r},t) \right\rangle$. $|\psi(\mathbf{r},t)|^2$ gives the particle density of the condensate, $\rho(\mathbf{r},t)$. Just as a laser is a classical state of the electromagnetic field (apart from the quantum noise), a BEC is a classical state of the atomic field.

Known as the Bogoliubov decomposition [22], this is most useful when the depletion of the condensate, measured by $\hat{\phi}$, is small. As the condensate is dilute and extremely cold, this can be assumed to be the case. At such low temperatures, the majority of the atoms occupy the ground state of the condensate and we expand in the lowest orders of $\hat{\phi}(\mathbf{r},t)$, giving a 'zeroth-order' mean-field theory for $\psi(\mathbf{r},t)$. Let us write the time evolution of $\hat{\Psi}(\mathbf{r},t)$, using the many-body Hamiltonian (3.1):

$$i\hbar\frac{\partial}{\partial t}\hat{\Psi}(\mathbf{r},t) = \left[-\frac{\hbar^2}{2m}\nabla^2 + V_{ext}(\mathbf{r}) + \int d\mathbf{r}'\hat{\Psi}^\dagger(\mathbf{r}',t)V(\mathbf{r}-\mathbf{r}')\Psi(\mathbf{r}',t)\right]\hat{\Psi}(\mathbf{r},t), \tag{3.2}$$

and then neglecting $\hat{\phi}$, we replace $\hat{\Psi}$ with ψ. Furthermore, the de Broglie wavelength is also very large compared to the range of the interatomic potential. This allows us to model the atom-atom interaction as the hard-sphere potential

$$V(\mathbf{r}-\mathbf{r}') = g\delta(\mathbf{r}-\mathbf{r}'); \tag{3.3}$$

a short-range delta-like term multiplied by a self-coupling constant g which is determined by the s-wave scattering length a and the atomic mass m:

$$g = \frac{4\pi\hbar^2 a}{m}, \tag{3.4}$$

provided $\bar{n}a \ll 1$, where $\bar{n}$ is the average density of the gas, a condition which generally holds.

Using this approximate potential in equation (3.2), we arrive at the following

closed-form equation for the weakly-interacting BEC

$$i\hbar\frac{\partial}{\partial t}\psi(\mathbf{r},t) = \left(-\frac{\hbar^2}{2m}\nabla^2 + V_{ext}(\mathbf{r}) + g|\psi(\mathbf{r},t)|^2\right)\psi(\mathbf{r},t). \tag{3.5}$$

This equation is known as the Gross-Pitaevskii equation, though it may also be referred to as a nonlinear Schrödinger equation. It describes the phenomena associated with BEC well, reproducing the pertinent features of superfluid systems such as condensate dynamics under expansion, phase-related interference effects of $\psi(\mathbf{r},t)$, propagation of collective excitations [23] and also vortices [24, 25], which we will meet again in a later chapter. It is, however, only valid provided the s-wave scattering length is much less than the average interatomic distance and that the condensate is well populated with $N \gg 1$.

3.3 Bose-Einstein condensate applications

Just as a laser emits coherent light, so can a BEC emit coherent waves of matter. A condensate can be forced to emit pulses of coherent atoms by applying a RF field which propels atoms to an untrapped state; the trap plays the role of the excited atom in a standard laser, the emitted atoms the photons. With each atom expelled from the trap, the probability grows that other atoms in the same state will join it, producing pulses of coherent matter - an atom laser [26]. Gravity then draws these matter pulses downwards. To show that these pulses are coherent, one can perturb two condensates with the same radio waves. The resulting matter pulses spread out as they fall, and where they overlap, an interference pattern occurs, demonstrating coherence. Progress towards a continuous-wave atom laser is ongoing today. An atom laser can be used for atom holography; the de Broglie wavelength of the atoms is much less than that of light, allowing the creation of high-resolution holographic images.

Atom interferometry is another potentially valuable application of atom lasers.

By appropriate manipulation of the confining potential, a condensate can be split into two parts. One part may be perturbed in some fashion, then recombined. Such processes can be performed on a very small scale, as on an atom chip, which consists of wires deposited on a chip, through which magnetic fields may be created to trap atoms very close to the surface. A great advantage of the use of BECs for atom interferometry is their slow speed; consequently, they are easy to deflect. High coherence is another important feature; the use of BECs could lead to devices with greatly increased sensitivity to gravity or EM fields, allowing investigation of quantum gravity.

Furthermore, as mentioned in the previous chapter, Bose-Einstein condensates offer an advantage when used in analogue black hole systems due to their low temperatures, leading to relative ease in detecting Hawking radiation compared to conventional fluids. They also have the advantage that the speed of sound in BECs can be on the order of a few millimetres per second. Let us consider some possible experimental configurations.

Laval nozzle

As a fluid flows through a nozzle, its speed increases as the nozzle becomes narrower. Once the nozzle is sufficiently narrow, the fluid flow will exceed the speed of sound in that fluid, creating a sonic event horizon. The most suitable type is known as a Laval nozzle or converging-diverging nozzle. The flow will arrange itself so that the sonic horizon occurs at the narrowest point of the nozzle. Such a system could be used as a laboratory analogue of a black hole [27, 28], using a Bose-Einstein condensate for the fluid and laser light to provide the constriction. We will meet the Laval nozzle again in Chapter 6, where I discuss issues relating to its simulation.

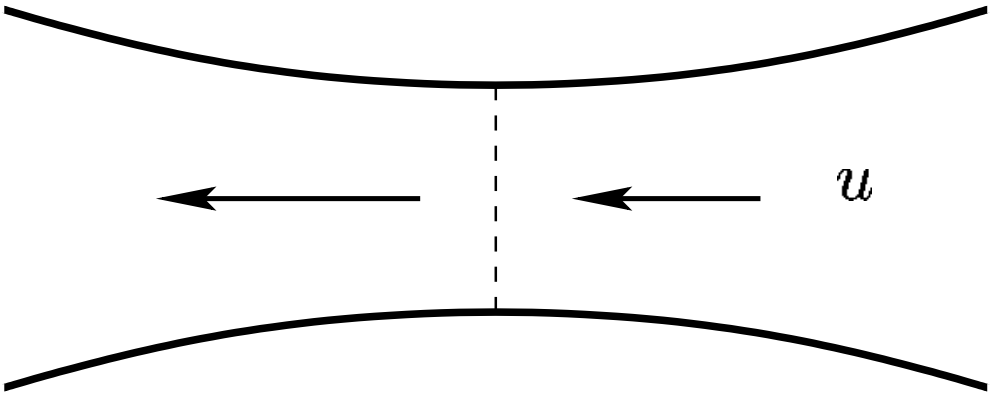

Figure 3.1: A Laval nozzle

Ring trap

A tightly-confined ring trap is essentially a (1+1)-dimensional system, dependent only on ω and t in radial co-ordinates. Supersonic flow in such a ring will generate a black hole-white hole horizon pair on either side of the supersonic region. The case of a Bose-Einstein condensate in such a trap has been simulated [29], indicating that the black hole-white hole pair is stable and could be experimentally feasible.

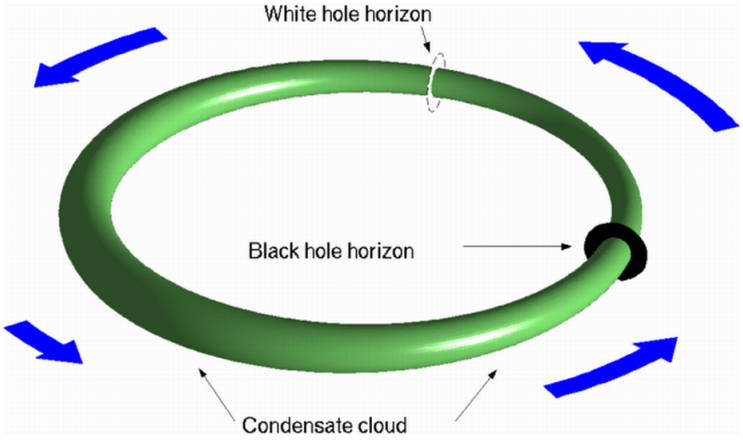

Figure 3.2: Black hole analogue in a ring trap

Sink-generated vortex

A vortex in a BEC, generated, for example, by an outcoupling laser, can indeed be considered an analogue black hole since it displays both event horizons and ergoregions. As one moves in towards the vortex core, the magnitude of the fluid velocity exceeds the speed of sound; in this region, the ergoregion, it is impossible to stand still without causing a sonic boom. Even nearer to the core, the radial component of the fluid velocity exceeds the speed of sound, making it impossible for any sound to escape; in other words, an event horizon. If the vortex motion is

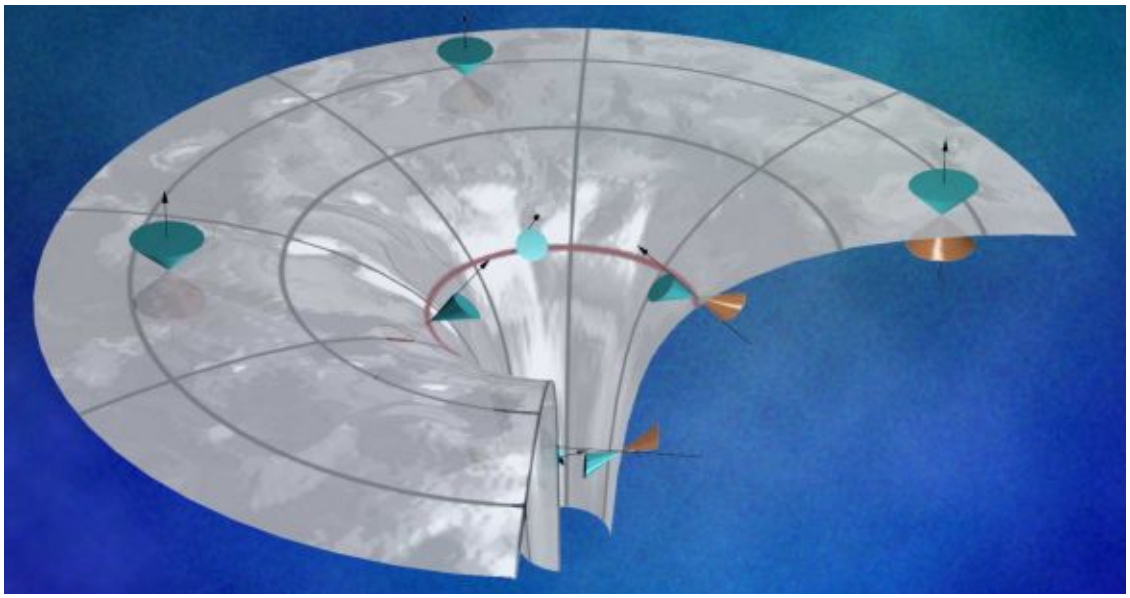

Figure 3.3: Sink-generated black hole analogue

completely radial the two regions coincide, but if there is swirling the two regions will separate. This is a fluid dynamic analogue of the general relativistic behaviour of the metric near a rotating black hole.

In addition to using this setup to create a sonic black hole, the ability to create light with extremely low group velocity, slow light [30], allows us to consider the possibility of optical black holes (distinct from the astronomical object!) [31]. Let us investigate in more detail how light can be slowed or even stopped.

Chapter 4

Slow light

The speed of light in a vacuum, c, is a well-known quantity, but in general the speed at which light travels depends on the medium it is in. The degree of velocity modification depends on the material's index of refraction n; the light's phase velocity - the rate at which the wave's phase travels - is given by the relation $v_{\text{phase}} = c/n$. We can also speak of the light's group velocity v_g, the rate at which changes in the shape of the wave's amplitude travel; $v_g = \partial\omega/\partial k$ where ω is the angular frequency and k, the wavenumber, is

$$k = n\frac{\omega}{c}, \tag{4.1}$$

hence

$$\begin{aligned} v_g &= \left(\frac{\partial k}{\partial \omega}\right)^{-1} = \left(\frac{n}{c} + \frac{\omega}{c}\frac{\partial n}{\partial \omega}\right)^{-1} \\ &= \frac{c}{n + \omega\frac{\partial n}{\partial \omega}} = \frac{c}{n_g}. \end{aligned} \tag{4.2}$$

We term n_g the group index. The light's travel can also be affected by its frequency, through dispersion; here the refractive index of the medium is a function of the light frequency, $n(\nu)$. The most familiar example of light being altered by a medium is the rainbow, where sunlight is split into its component frequencies

after passing through a water droplet and being refracted.

Slow light refers to light whose velocity is on the order of metres per second or even less [30]. Clearly, to obtain such a fantastic reduction in phase velocity, one would need a correspondingly large refractive index, which is not simple to achieve. We turn instead to a quantum mechanical trick which causes light to take a very long time to traverse a given distance through its constant absorption and reemission by atoms of the material. A pulse of light can be considered as the point at which the various frequency components which comprise it are in phase. Using this trick, these frequency components are dispersed, causing the place where they are in phase to effectively be shifted back, hence slowing the beam; it is the group velocity of the light pulse which is slowed as opposed to the phase velocity.

This method is known as Electromagnetically Induced Transparency (EIT) [32]; it is frequently used in dilute alkali vapours and has also been used in Bose-Einstein condensates [30]; as we have seen, it also has the potential for the creation of black hole analogues. Ultracold atoms [33], with their relatively small vibrational motion, allow properties where slow light interaction leads to motion, such as the Iordanskii force, to be investigated with greater ease; we will discuss such effects in greater detail in a later chapter.

4.1 Electromagnetically Induced Transparency

Consider a cloud of atoms with a three-level atomic system. If we send in a beam of probe light with a frequency equal to the $|1\rangle \rightarrow |3\rangle$ transition, ω_{13}, it will be absorbed by the atoms then spontaneously reemitted at random, removing any interesting features of the initial light pulse. However, we can modify the properties of the atom cloud by shining a control beam on it which couples levels $|2\rangle$ and $|3\rangle$ together.

Initially the atoms are in their ground state $|1\rangle$ and so the control beam will not

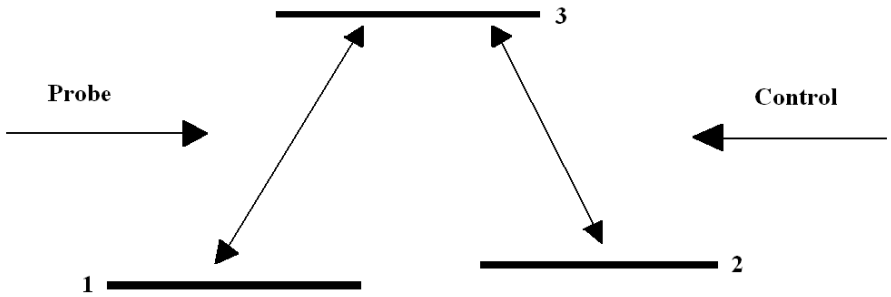

Figure 4.1: A three-level system under Electromagnetically Induced Transparency. Levels $|2\rangle$ and $|3\rangle$ are coupled by the control beam, strongly modifying the optical properties of the atom for a probe beam tuned to the $|1\rangle \rightarrow |3\rangle$ transition.

be absorbed. With the advent of the probe beam, the atoms are put into a superposition of states $|1\rangle$ and $|2\rangle$, known as a dark state, with neither the absorption of the probe nor control beams able to dominate; in other words, destructive quantum interference between the paths of the transition process occurs, which causes the atom to be transparent in a frequency region where it would otherwise be opaque, hence Electromagnetically Induced Transparency (EIT). In the vicinity of the transparent frequency $\omega_0 = \omega_{13} = \omega_{12} + \omega_{23}$, the material is extremely dispersive since the interference is not completely destructive, being highly sensitive to the frequency.

As the atom cloud interacts with the light, the dominant relaxation mechanisms are from $|3\rangle \rightarrow |2\rangle$ and $|3\rangle \rightarrow |1\rangle$, while $|2\rangle \rightarrow |1\rangle$ is relatively rare; this is due to the spontaneous emission rate being proportional to the cube of the transition frequencies, ω_{12} normally being on the order of 10^6 smaller than ω_{23} and ω_{13}. Let us now consider the light-matter interaction in greater detail.

The light sees the atoms as dipoles [34], the energy density of the light-matter interaction being $-\mathbf{P} \cdot \mathbf{E}$, where $\mathbf{P}$ is the matter polarization and $\mathbf{E}$ the electric field. The Lagrangian is

$$\mathcal{L} = \frac{\epsilon_0}{2}(E^2 - c^2 B^2) + \mathbf{P} \cdot \mathbf{E} + \mathcal{L}_A, \tag{4.3}$$

the last term referring to the internal dynamics of the atoms. Representing $\mathbf{E}$ and $\mathbf{B}$ in terms of the vector potential $\mathbf{A}$ in the Coulomb gauge [34],

$$\mathbf{E} = -\partial_t \mathbf{A},\ \mathbf{B} = \nabla \times \mathbf{A},\ \nabla \cdot \mathbf{A} = 0. \tag{4.4}$$

Assuming the electric and magnetic fields vary only in z and that the polarization is fixed so that we consider only one component A of $\mathbf{A}$, this gives the Lagrangian

$$\mathcal{L} = \frac{\epsilon_0}{2}((\partial_t A)^2 - c^2(\partial_z A)^2) - P\partial_t A + \mathcal{L}_A, \tag{4.5}$$

and the Euler-Lagrange equation leads to the wave equation

$$(\partial_t^2 - c^2\partial_z^2)E = -\frac{1}{\epsilon_0}\partial_t^2 P. \tag{4.6}$$

Considering a two-level system for the moment, we write its Hamiltonian as

$$\begin{aligned} \hat{H} &= \hbar\omega_{12}|2\rangle\langle 2| - \frac{\kappa_{12}}{2}\left(\hat{A} + \hat{A}^\dagger\right)E, \\ \hat{A} &= |1\rangle\langle 2|, \end{aligned} \tag{4.7}$$

where $|1\rangle$ and $\langle 2|$ are the ground and excited states respectively and κ_{12} is the atomic dipole moment, which is a real number for transitions between bound states. The transition operator $\hat{A}$ oscillates with positive frequencies near ω_{12} in the Heisenberg picture; thus we can say that $\hat{A}$ couples entirely to the negative-frequency component of the electric field, $E^{(-)}$, while $\hat{A}^\dagger$ couples to the positive-frequency component $E^{(+)}$. This gives the effective Hamiltonian

$$\hat{H} = \hbar\omega_{12}|2\rangle\langle 2| - \frac{\kappa_{12}}{2}\left(\hat{A}E^{(-)} + \hat{A}^\dagger E^{(+)}\right). \tag{4.8}$$

Returning to the three-level system, we can write its Hamiltonian in a similar

fashion as

$$\hat{H} = \hbar\omega_{12}|2\rangle\langle 2| + \hbar\omega_{13}|3\rangle\langle 3| - \frac{1}{2}\sum_a \kappa_a \left(\hat{A}_a E^{(-)} + \hat{A}_a^\dagger E^{(+)}\right), \; a = 1, 2 \qquad (4.9)$$

where

$$\kappa_1 = \kappa_{13}, \; \kappa_2 = \kappa_{23},$$
$$\hat{A}_1 = |1\rangle\langle 3|, \hat{A}_2 = |2\rangle\langle 3|. \qquad (4.10)$$

In the absence of relaxation and taking into account only those frequency components of the probe and control light $E_p^{(\pm)}$ and $E_c^{(\pm)}$ that fit the level structure, we can write this in matrix form as

$$\hat{H} = \begin{bmatrix} 0 & 0 & -\frac{1}{2}\kappa_{13}E_p^{(-)} \\ 0 & \hbar\omega_{12} & -\frac{1}{2}\kappa_{23}E_c^{(-)} \\ -\frac{1}{2}\kappa_{13}E_p^{(+)} & -\frac{1}{2}\kappa_{23}E_c^{(+)} & \hbar\omega_{13} \end{bmatrix}. \qquad (4.11)$$

Let us assume that ω_c is exactly equal to ω_{23}. In a linear response regime, we can consider the probe light as being composed of monochromatic waves. The probe field can be described by the Rabi frequency Ω_p,

$$\Omega_p e^{-i\omega_p t} = \frac{\kappa_{13}}{\hbar}E_p^{(+)}. \qquad (4.12)$$

The control light can be described similarly;

$$\Omega_c e^{-i\omega_c t} = \frac{\kappa_{23}}{\hbar}E_c^{(+)}. \qquad (4.13)$$

These Rabi frequencies give the time scales at which light-induced atomic transitions occur, the control field being dominant. Under the influence of relaxation, the atoms follow the light fields and eventually reach a stationary state. The

Lindblad operators $\hat{A}_1$, $\hat{A}_2$ describe the relaxation processes and occur at rates γ_1 and γ_2.

To investigate this state, let us turn to the interaction picture. We use a partial Hamiltonian

$$\hat{H}_0 = \hbar \begin{bmatrix} 0 & 0 & 0 \\ 0 & \omega - \omega_c & 0 \\ 0 & 0 & \omega \end{bmatrix}. \tag{4.14}$$

which describes the interaction and is separated from the total evolution of the density matrix $\hat{\rho}$. According to Lindblad's theorem [35] the density matrix evolves in the Schrödinger picture according to the master equation [36],

$$\frac{d\hat{\rho}}{dt} = \frac{i}{\hbar}[\hat{\rho}, \hat{H}] - \sum_a \gamma_a \left(\hat{A}_a^\dagger \hat{A}_a \hat{\rho} - 2\hat{A}_a \hat{\rho} \hat{A}_a^\dagger + \hat{\rho} \hat{A}_a^\dagger \hat{A}_a \right), \tag{4.15}$$

provided it is normalized and non-negative. The transformed density matrix $\tilde{\rho}$ is given by

$$\tilde{\rho} = \hat{U}_0^\dagger \hat{\rho} \hat{U}_0,\ \hat{U}_0 = \exp\left(-\frac{i}{\hbar} \hat{H}_0 t \right). \tag{4.16}$$

The commutation relations between the terms $\hat{A}$ and $\hat{H}_0$ are

$$[\hat{A}_x, \hat{H}_0] = \hbar \omega_x \hat{A}_x, \tag{4.17}$$

and so $\hat{U}_0^\dagger \hat{A}_x \hat{U}_0 = \hat{A}_x \exp(-i\omega_t)$ and the disspative part of the master equation remains the same when we consider interactions. The Hamiltonian transforms as

$$\tilde{H} = \hat{U}_0^\dagger \hat{H} \hat{U}_0 - \hat{H}_0 \tag{4.18}$$

giving us

$$\tilde{H} = -\hbar \begin{bmatrix} 0 & 0 & \frac{1}{2}\Omega_p^* \\ 0 & \omega - \omega_0 & \frac{1}{2}\Omega_c^* \\ \frac{1}{2}\Omega_p & \frac{1}{2}\Omega_c & \omega - \omega_0 \end{bmatrix}, \tag{4.19}$$

which is time-independent.

In a stationary state, atomic relaxation should be balanced by the optical transitions;

$$\frac{i}{\hbar}[\tilde{\rho}, \tilde{H}] = \sum_{a=1}^{2} \gamma_a \left(\hat{A}_a^\dagger \hat{A}_a \hat{\rho} - 2\hat{A}_a \hat{\rho} \hat{A}_a^\dagger + \hat{\rho} \hat{A}_a^\dagger \hat{A}_a \right). \tag{4.20}$$

Provided $|\Omega_c| \gg |\omega - \omega_0|$ and also dominates the other timescales in the system, we can write the solution of the above as

$$\tilde{\rho} = \begin{bmatrix} 1 - \frac{|\Omega_p|^2}{|\Omega_c|^2} & -\frac{\Omega_p^*}{\Omega_c^*} & \frac{2(\omega-\omega_0)}{|\Omega_c|^2}\Omega_p^* \\ -\frac{\Omega_p}{\Omega_c} & \frac{|\Omega_p|^2}{|\Omega_c|^2} & 0 \\ \frac{2(\omega-\omega_0)}{|\Omega_c|^2}\Omega_p & 0 & 0 \end{bmatrix} \tag{4.21}$$

This allows us to calculate the matter polarization for a given number of atoms n_A and hence the spectral susceptibility, which for positive frequency here is

$$\tilde{\chi} = \frac{2\alpha}{\omega_0}(\omega - \omega_0), \tag{4.22}$$

where α is

$$\alpha = \frac{n_A}{2} \frac{\kappa_{13}^2}{\kappa_{23}^2} \frac{\hbar\omega_0}{\epsilon_0 |E_c|^2}. \tag{4.23}$$

Provided that the properties do not vary to any great extent over an optical wavelength, we can describe light pulse propagation by the dispersion relation obtained from the wave equation by Fourier transformation

$$k^2 = \frac{\omega^2}{c^2}(1 + \tilde{\chi}). \tag{4.24}$$

Light pulses propagate as particles with Hamiltonian ω and momentum k, subject to Hamilton's equations

$$\frac{\mathrm{d}k}{\mathrm{d}t} = -\frac{\partial\omega}{\partial z}, \frac{\mathrm{d}z}{\mathrm{d}t} = \frac{\partial\omega}{\partial t}. \tag{4.25}$$

The velocity of the 'light particle', $\mathrm{d}z/\mathrm{d}t$, is the group velocity of the light pulse,

$$v_g = \frac{c}{n + \frac{\omega}{2n}\frac{\partial \tilde{\chi}}{\partial \omega}}, \quad n = \sqrt{1+\tilde{\chi}} \tag{4.26}$$

At the resonance frequency ω_0 in the EIT case, this reduces to

$$v_g = \frac{c}{1+\alpha} = \frac{c}{n_g}, \tag{4.27}$$

so we can say $\alpha = n_g - 1 \approx n_g$. In other words, reducing the control light's intensity slows the light pulse, contrary to what one might expect. Indeed, actually turning the control beam off 'freezes' the light pulse inside the medium, encoding it onto the atoms; it can be 'unfrozen' by switching on the control light once again [37, 38].

4.2 Dark state dynamics

Once an atom has been prepared in the state (4.21), how does it behave when the control and probe fields are then varied [39]? The state described by $\tilde{\rho}$ is statistically pure, meaning

$$\mathrm{tr}\{\hat{\rho}^2\} = 1. \tag{4.28}$$

If this is the case, the density matrix is

$$\hat{\rho} = |\psi_0\rangle\langle\psi_0|, \tag{4.29}$$

a single state vector [36], where

$$|\psi_0\rangle = \hat{U}_0 N_0 \left(|1\rangle - \frac{\Omega_p}{\Omega_c}|2\rangle + \frac{2(\omega-\omega_0)}{|\Omega_c|^2}\Omega_p|3\rangle \right). \tag{4.30}$$

Here

$$\hat{U}_0 = \begin{bmatrix} 1 & 0 & 0 \\ 0 & e^{-i\omega_{12}t} & 0 \\ 0 & 0 & e^{-i\omega_0 t} \end{bmatrix}, \tag{4.31}$$

$$\frac{\Omega_p}{\Omega_c} = \left|\frac{\Omega_p}{\Omega_c}\right| e^{i\theta}, \tag{4.32}$$

$$N_0 = \left(1 + \frac{|\Omega_p|^2}{|\Omega_c|^2}\right)^{-1/2}. \tag{4.33}$$

As we can see, this stationary state depends only on the Hamiltonian $\tilde{H}$. Provided the $|3\rangle$ component is small, changes in probe or control intensity will not cause further relaxation. Once the atom is in a pure state with a minimally populated top level, the purity will not change when it is evolved using the master equation (4.15),

$$\mathrm{d}(\mathrm{tr}(\hat{\rho}^2)) = 2\mathrm{tr}(\hat{\rho}\mathrm{d}\hat{\rho}) = 4[\gamma_1(1-\rho_{11}) + \gamma_2(1-\rho_{22})]\rho_{33}\mathrm{d}t. \tag{4.34}$$

We call this state a dark state; having adapted to the light fields, it is not prone to dissipation. Since the relaxation processes $\hat{A}_1$ and $\hat{A}_2$ do not operate between $|1\rangle$ and $|2\rangle$ we need only consider these levels to find the dark state dynamics when the probe and control fields vary. A state $|\psi\rangle$ which correctly describes the dynamics given by the master equation in the $|1\rangle - |2\rangle$ subspace will describe $\langle 3|\psi\rangle$ correctly as well. Such a state is

$$|\psi\rangle = \hat{U}_0 N \left(|1\rangle - \frac{\Omega_p}{\Omega_c}|2\rangle + \frac{2N_0^2}{\Omega_c^*} i\partial_t \frac{\Omega_p}{\Omega_c}|3\rangle\right), \tag{4.35}$$

where

$$N = N_0 \exp\left(-i\int \frac{|\Omega_p|^2 \mathrm{d}\theta}{|\Omega_p|^2 + |\Omega_c|^2}\right). \tag{4.36}$$

When $|\Omega_c|$ dominates the timescales of the system, $|\psi\rangle$ agrees with $|\psi_0\rangle$. We can

see $|\psi\rangle$ satisfies

$$i\hbar\partial_t|\psi\rangle = \hat{H}|\psi\rangle + i\hbar\partial_t\langle 3|\psi\rangle|3\rangle \tag{4.37}$$

since

$$\partial_t N = -NN_0^2\frac{\Omega_p^*}{\Omega_c^*}\partial_t\frac{\Omega_p}{\Omega_c},\ \partial_t N\frac{\Omega_p}{\Omega_c} = NN_0^2\partial_t\frac{\Omega_p}{\Omega_c}. \tag{4.38}$$

The atom stays in the dark state as long as the $|3\rangle$ component remains negligible. After initially being prepared in the dark state, the atom follows dynamically without relaxation [39]. The positive-frequency component of the matter polarization generated by the atoms of the dark state, $P^{(+)}$, is

$$\begin{aligned} P^{(+)} &= \frac{n_A}{2}\kappa_{31}\langle 3|\psi\rangle\langle\psi|1\rangle \\ &= \frac{n_A}{2}\kappa_{31}e^{-i\omega_0 t}N_0^4\frac{2}{\Omega_c^*}i\partial_t\frac{\Omega_p}{\Omega_c} \\ &= n_A\frac{\kappa_{31}^2}{\hbar}\frac{N_0^4}{|\Omega_c|^2}\left(i\partial_t - \omega_0 - i\frac{(\partial_t|\Omega_c|)}{|\Omega_c|} + \dot{\theta}_c\right)E_P^{(+)}, \end{aligned}$$

where $\theta_c = \arg\Omega_c$.

For simplicity, let Ω_c be real; if not, the phase of the control field can be incorporated in the phase of the electric field as long as θ_c changes slowly with respect to ω_0 without changing the wave equation (4.6). This leads to the expression

$$\frac{1}{\epsilon_0}\partial_t^2 P^{(+)} \approx -N_0^4\alpha 2\omega_0\left(i\partial_t - \omega_0 i\frac{\dot{\alpha}}{2\alpha}\right)E_p^{(+)}. \tag{4.39}$$

Approximating as follows,

$$2\omega_0(i\partial_t - \omega_0)E_p^{(+)} \approx (i\partial_t + \omega_0)(i\partial_t - \omega_0)E_p^{(+)} = -(\partial_t^2 + \omega_0^2)E_p^{(+)} \tag{4.40}$$

we obtain an equation valid for both $E_p^{(+)}$ and $E_p^{(-)}$,

$$(\partial_t^2 - c^2\partial_z^2 + N_0^4(\partial_t\alpha\partial_t + \alpha\omega_0^2))E_p = 0 \tag{4.41}$$

from (4.6). The N_0^4 factor is a nonlinear effect of the medium, but when $|\Omega_p|^2/|\Omega_c|^2$ is small, the medium responds linearly:

$$(\partial_t(1+\alpha)\partial_t - c^2\partial_z^2 + \alpha\omega_0^2)E_p = 0 \tag{4.42}$$

Now that we have investigated the links between different methods of modelling reality, Bose-Einstein condensates and slow light, let us turn to numerical simulations of condensed matter systems, both as black hole analogues and otherwise.

Chapter 5

The Perfectly Matched Layer and its use

5.1 The Perfectly Matched Layer

Perhaps the foremost problem when simulating physical behaviour, such as the supersonic flow of a BEC, is how to handle behaviour at the boundaries of the system, especially where we wish to consider the case of an open system[1]. In such cases, periodic boundary conditions are often inappropriate to reduce the computational domain. A possible solution is to simply use a very large, empty computational domain, with the region of interest sitting like an island in the midst of nothingness. However, this is inefficient and in general not practical, due to memory storage constraints and the excessive runtime such a simulation would involve; in numerical simulations one should focus on the most relevant parts of the physical processes involved and not spend computational resources on the continuation of the wave propagation. A more practical approach is the use of an absorbing boundary condition (ABC) to truncate the domain and absorb incoming waves. An efficient ABC will save computer memory and processing time and will

[1]Material from this chapter originally appeared in J. Opt. B. [40].

minimize spurious numerical reflections from the domain truncation; alternatives, such as complex potentials, may cause reflections unless they are artificially fine-tuned to the specific processes that are simulated.

The Perfectly Matched Layer [41], or PML, is an absorbing boundary condition which is reflectionless in theory, though some small reflection does occur in practice due to discretization. The magnitude of this reflection is considerably smaller than that of other ABCs, however (for one comparison, see [42]). It has been extensively used in the field of electromagnetics (see [43]-[47], for example) and has also found application in acoustical and geophysical work [48]-[52].

The concept of the PML for nonlinear and matter waves is similar to that for linear wave propagation, as in the original application to electromagnetic waves. The essential idea is the use of transformations which map propagating solutions onto exponentially decaying evanescent waves in complex space. Thus, waves travelling in the PML change from propagation in real space to propagation in imaginary space. The idea of using complex space for waves originated with Deschamps [53] and the PML was first interpreted as a complex coordinate stretching by Chew and Weedon [54]. Let us investigate how these ideas can be applied to nonlinear and matter waves. Consider first the standard linear Schrödinger equation in one dimension,

$$i\frac{\partial\psi}{\partial t} = -\frac{1}{2m}\frac{\partial^2\psi}{\partial x^2}, \tag{5.1}$$

which can be written as

$$i\frac{\partial\psi}{\partial t} = -\frac{1}{2n}\frac{\partial}{\partial x}\frac{1}{n}\frac{\partial\psi}{\partial x}, \tag{5.2}$$

where m, the mass, has been split into two spatially dependent functions n. Suppose that n changes value from 1 at $x = \infty$ to i at $x = -\infty$. Equation (5.2) has the general solution

$$\psi = \int_0^\infty A(\omega)\exp\left(\pm i\int k dx - i\omega t\right)d\omega,\ k = \pm n\sqrt{2\omega}, \tag{5.3}$$

where the term inside the exponential is positive for waves moving to the left and negative for waves moving to the right. Therefore, the wave will decay rapidly without reflection. The region where n changes from real to purely imaginary values defines the PML. We can choose n to be, for example,

$$n = \exp\left[\pm i\frac{\pi}{4}\left(1 - \tanh\frac{x - x_0}{a}\right)\right], \tag{5.4}$$

where the exponential is positive or negative depending on the direction of propagation of the waves in question. x_0 is the position where the PML starts and a is a parameter which determines the sharpness of the transition between 1 and i which should be reasonably gradual, though my simulations, described below, indicate that the transition may be quite steep without any serious effects. The introduction of n is equivalent to making the transformation

$$\xi = \int n \mathrm{d}x \tag{5.5}$$

and writing

$$i\frac{\partial\psi}{\partial t} = -\frac{1}{2}\frac{\partial^2}{\partial\xi^2}\psi. \tag{5.6}$$

In essence, we have transformed to a coordinate system that causes waves to exponentially decay as they approach $-\infty$.

To consider nonlinear waves such as optical solitons in fibres [55] or Bose-Einstein condensates, let us write a nonlinear Schrödinger equation, after scaling through proper coefficient choices,

$$i\frac{\partial\psi}{\partial t} = -\frac{1}{2n}\frac{\partial}{\partial x}\frac{1}{n}\frac{\partial\psi}{\partial x} + \epsilon|\psi|^2\psi,\ \epsilon = \pm 1. \tag{5.7}$$

If ϵ is positive, the equation represents repulsive interactions, such as in a dark soliton in a Bose-Einstein condensate; if negative, the equation represents attractive interactions, as in a bright matter wave soliton or the anomalous dispersion

required for optical solitons.

The PML can be extended to deal with nonlinear wave propagation provided the incoming wavefront is close to zero. If this condition is met, the PML acts to keep the incoming wave small and so the system is approximately in the linear regime, allowing us to perform a coordinate transformation in the same fashion as Eq. (5.5); we can write

$$i\frac{\partial\psi}{\partial t} = -\frac{1}{2}\frac{\partial^2}{\partial\xi^2}\psi + \epsilon|\psi|^2\psi. \tag{5.8}$$

In practice, nonlinearities generate slightly higher reflection from the PML than in the case of purely linear propagation, but during simulations the reflectivity was always $< 10^{-4}$ and had negligible influence on the simulation accuracy.

Transforming the nonlinear Schrödinger equation in this fashion can be useful in the simulation of a Laval nozzle (see Section 3.3). This system is difficult to model computationally, since the process of turning a supersonic flow into a subsonic one is even more unstable than the converse and so periodic boundary conditions are unsuitable. Placing a PML at the supersonic end of the system allows us to model the condensate flow with much greater physical accuracy, by absorbing the supersonic matter waves and so simulating their propagation into free space. Similarly, the PML technique could be applied to the modelling of soliton propagation in glass fibres [55] or in a BEC [56]. Let us discuss some issues relating to numerical implementation of the PML.

5.2 Numerical implementation of the GPE with PML terms

In a diffusion equation of the form

$$\frac{\partial u}{\partial t} = \frac{\partial}{\partial x}\alpha(x)\frac{\partial u}{\partial x} \tag{5.9}$$

where the diffusion coefficient α is not constant in space, the discretization scheme must take this into account. One method of doing this is to change variables by letting

$$\gamma = \int \frac{dx}{\alpha(x)}, \tag{5.10}$$

which means that (5.9) becomes

$$\frac{\partial u}{\partial t} = \frac{1}{\alpha(\gamma)} \frac{\partial^2 u}{\partial \gamma^2}. \tag{5.11}$$

This requires an analytically tractable form for $\alpha(x)$, however, so an alternate method is to discretize the diffusion coefficient with the other terms:

$$\begin{aligned} \frac{u_i^{t+1} - u_i^t}{\Delta t} = \frac{1}{2\Delta x^2} \Big(& \alpha_{i+1/2} \left((u_{i+1}^{t+1} - u_i^{t+1}) + (u_{i+1}^t - u_i^t) \right) \\ - \ & \alpha_{i-1/2} \left((u_i^{t+1} - u_{i-1}^{t+1}) + (u_i^t - u_{i-1}^t) \right) \Big), \end{aligned} \tag{5.12}$$

where $\alpha_{i+1/2} = \alpha(x_{i+1/2})$.

Schrödinger-type equations must also be discretized in a fashion that is consistent with underlying physical constraints. In this case, we require that the norm is conserved, *i.e.*

$$\int_{-\infty}^{\infty} |\psi|^2 = 1. \tag{5.13}$$

Consider the dimensionless 1D Schrödinger equation discretized using a fully implicit, first-order in time method (Section 1.2.3):

$$i \frac{\psi_x^{t+1} - \psi_x^t}{\Delta t} = - \frac{\psi_{x+1}^{t+1} - 2\psi_x^{t+1} + \psi_{x-1}^{t+1}}{2\Delta x^2} + V_x \psi_x^{t+1} \tag{5.14}$$

As we found, this discretization scheme is stable for any value of Δx and Δt, but this approach has a more subtle problem.

The dimensionless 1D Schrödinger equation can also be written as

$$i\frac{\partial\psi}{\partial t} = \hat{H}\psi; \quad \hat{H} = -\frac{\partial^2}{\partial x^2} + V(x). \tag{5.15}$$

The solution to this equation is

$$\psi(x,t) = e^{-i\hat{H}t}\psi(x,0). \tag{5.16}$$

This is approximated by the fully implicit difference scheme as

$$\psi_x^{t+1} = (1 + i\hat{H}\Delta t)^{-1}\psi_x^t, \tag{5.17}$$

$\hat{H}$ being discretized in a centred fashion, which is not unitary. Similarly, the FTCS method (Section 1.2.1) is approximated as

$$\psi_x^{t+1} = (1 - i\hat{H}\Delta t)\psi_x^t \tag{5.18}$$

which, again, is not unitary.

To obtain a unitary finite-difference representation, we use Cayley's form for the discretization of $\exp(i\hat{H}t)$,

$$e^{-i\hat{H}t} \approx \frac{1 - \frac{1}{2}i\hat{H}\Delta t}{1 + \frac{1}{2}i\hat{H}\Delta t} \tag{5.19}$$

which is unitary and which we have met before as the Crank-Nicholson discretization scheme (Section 1.2.4), as we can see if we write

$$(1 + \frac{1}{2}i\hat{H}\Delta t)\psi_x^{t+1} = (1 - \frac{1}{2}i\hat{H}\Delta t)\psi_x^t \tag{5.20}$$

The Crank-Nicholson scheme is therefore the natural one for Schrödinger-type problems where the norm must be conserved.

The above scheme is the one chosen to solve the Gross-Pitaevskii equation. The PML term takes the role of the diffusion coefficient, making the system to be solved

$$\begin{aligned} i\frac{\psi_x^{t+1}-\psi_x^t}{\Delta t} = &-\frac{1}{2}\frac{\nu_x}{2\Delta x^2}\left[\nu_{x+\frac{1}{2}}\left(\psi_{x+1}^{t+1}-\psi_x^{t+1}\right)-\nu_{x-\frac{1}{2}}\left(\psi_x^{t+1}-\psi_{x-1}^{t+1}\right)\right. \\ &\left.+\ \nu_{x+\frac{1}{2}}\left(\psi_{x+1}^{t}-\psi_x^{t}\right)-\nu_{x-\frac{1}{2}}\left(\psi_x^{t}-\psi_{x-1}^{t}\right)\right] \\ &+\frac{|\psi_x|^2}{2}\left(\psi_x^{t+1}+\psi_x^t\right), \end{aligned} \tag{5.21}$$

where $\nu_x = 1/n(x)$. The tridiagonal system of equations so produced is solved using the tridiagonal matrix algorithm, also known as the Thomas algorithm [57].

5.2.1 The Thomas algorithm

A general system of tridiagonal equations can be expressed in the form

$$\begin{aligned} b_1u_1 + c_1u_2 &= d_1 \\ a_iu_{i-1} + b_iu_i + c_iu_{i+1} &= d_i,\ i = 2, 3 \ldots n-1. \\ a_nu_{n-1} + b_nu_n &= d_n. \end{aligned}$$

We transform this system to one of upper bidiagonal form by Gaussian elimination - the subtraction of a suitable multiple of each equation from the following equations. Let us denote the coefficients of this new system a', b', c', d'. Note that

$$a_i' = 0,\ \ i = 2,\ 3,\ \ldots n \tag{5.22}$$

$$b_i' = 1,\ \ i = 1,\ 2,\ \ldots n. \tag{5.23}$$

We obtain c_i' and d_i' by calculating

$$c_i' = \frac{c_1}{b_1},\ d_i' = \frac{d_1}{b_1} \tag{5.24}$$

$$c_{i+1}' = \frac{c_{i+1}}{b_{i+1} - a_{i+1}c_i'} \tag{5.25}$$

$$d_{i+1}' = \frac{d_{i+1}}{b_{i+1} - a_{i+1}c_i'} \tag{5.26}$$

where $i = 1,\ 2,\ \ldots n-1$ and $c_n = 0$.

The nth equation is then

$$u_n = d_n' \tag{5.27}$$

and we can obtain the other solutions by the prescription

$$u_i = d_i' - c_i' u_{i+1},\ i = n-1,\ n-2,\ \ldots 1. \tag{5.28}$$

Of course, for this method as presented to work, b_1 cannot be zero, nor can $b_{i+1} - a_{i+1}c_i'$. If these terms are zero, we solve for u_2 or u_{i+2} respectively. Furthermore, if $|b_{i+1} - a_{i+1}c_i'|$ is small, pivoting should be employed to reduce round-off error. However, this is usually not the case for the Gross-Pitaevskii equation and, in general, no special action need be taken.

5.2.2 Extension to 2+1 Dimensions

To deal with the Gross-Pitaevskii equation in two dimensions, additional measures must be employed as otherwise the system is no longer tridiagonal, making it much more difficult to solve. To circumvent this problem, we turn to the alternating-direction implicit (ADI) method, first introduced for parabolic equations by Douglas, Peaceman and Rachford [58].

The key concept of ADI methods is the use of alternating row and column it-

erations. First, the system of finite difference equations in question is arranged into linear equations possessing a tridiagonal form. For two space dimensions, the time-step is also split into two; in the first part of the time-step, one space variable is evaluated at advanced time, which gives an intermediate value, $\psi^{t+1/2}$. In the second, using the intermediate value and evaluating the other space variable at advanced time gives the final value ψ^{t+1}. The difference equations for the simple diffusion equation $\partial_t \psi = \partial_x^2 \psi + \partial_y^2 \psi$ become

$$\frac{\psi_{i,j}^{t+1/2} - \psi_{i,j}^{t}}{\Delta t/2} = \nabla_x^2 \psi_{i,j}^{t+1/2} + \nabla_y^2 \psi_{i,j}^{t}, \tag{5.29}$$

$$\frac{\psi_{i,j}^{t+1} - \psi_{i,j}^{t+1/2}}{\Delta t/2} = \nabla_x^2 \psi_{i,j}^{t+1/2} + \nabla_y^2 \psi_{i,j}^{t+1}, \tag{5.30}$$

where ∇_x represents the standard second-order discretization for $\partial^2/\partial x^2$ and ∇_y similarly for y. The difference equations are then solved as normal using the Thomas algorithm.

The eigenfunctions for this problem are

$$v_{i,j,n}^{p,q} = \rho_n \sin(p\pi i \Delta x) \sin(q\pi j \Delta y)$$

and we can use von Neumann stability analysis to give the stability ratios for the first and second steps

$$\frac{\rho_{n+1/2}}{\rho_n} = \frac{1 - 4r_y \sin^2(q\pi \Delta y/2)}{1 + 4r_x \sin^2(p\pi \Delta x/2)} \tag{5.31}$$

$$\frac{\rho_{n+1}}{\rho_{n+1/2}} = \frac{1 - 4r_x \sin^2(p\pi \Delta x/2)}{1 + 4r_y \sin^2(q\pi \Delta y/2)} \tag{5.32}$$

where $r_x = \Delta t/\Delta x^2$ and $r_y = \Delta t/\Delta y^2$. While, individually, these steps are conditionally stable, the absolute value of the product of the stability ratios is ≤ 1 for any time step, making the composite process unconditionally stable. This method is also second-order accurate in both space and time.

5.2.3 The 2D PML

A two-dimensional simulation often necessitates a two-dimensional PML; the easiest method of accomplishing this is to have separate x and y absorbing layers, as in

$$i\frac{\partial\psi}{\partial t} = -\frac{1}{2}\left(\frac{\partial^2}{\partial\xi^2} + \frac{\partial^2}{\partial\chi^2}\right)\psi, \tag{5.33}$$

where

$$\chi = \int m\mathrm{d}y \tag{5.34}$$

and m describes an appropriate PML. Frequently, we wish a double-sided PML in the y-direction to absorb waves exiting the computational domain at the $\pm y$ boundaries; the m that describes this PML is

$$m = \exp\left[i\frac{\pi}{4}\left(1 - \tanh\frac{y - y_0}{a}\right)\right]\exp\left[i\frac{\pi}{4}\left(1 + \tanh\frac{y + y_0}{a}\right)\right] \tag{5.35}$$

As the PML is strongly directional, waves travelling in the x-direction through a y-aligned PML will not be strongly affected, and vice versa.

Let us now observe the benefits of the PML for numerical simulations of 1D BECs with attractive and repulsive interaction. For the simulations below, the GPE was scaled such that $\hbar = g = 1$ and the space discretization length Δx was normally 0.1.

5.2.4 Attractive interaction: Travelling soliton

In a 1D computational domain 100 discretization lengths wide, travelling solitons are inserted into the system, generated by a boundary condition on the right-hand side; if ψ_s^t is the time-dependent description of a soliton, the discretization at the

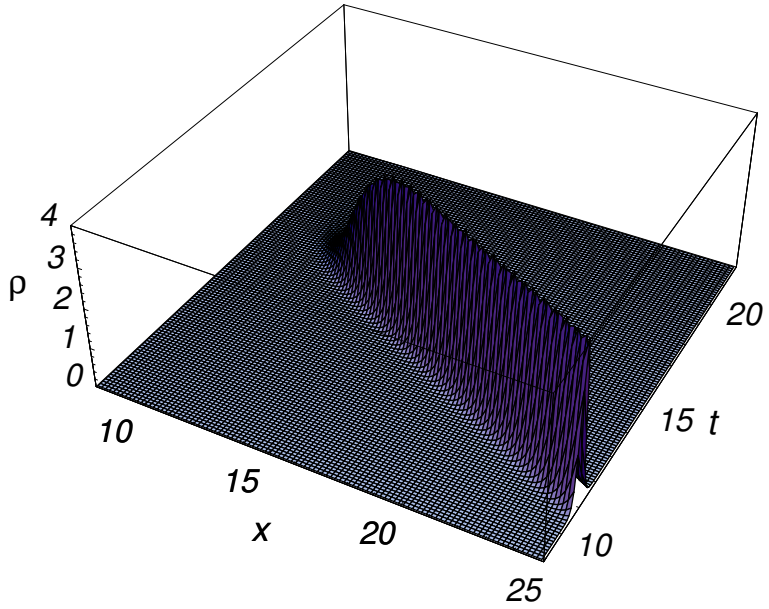

Figure 5.1: Once the soliton reaches the PML it begins to be absorbed, the peak value of ρ dropping sharply.

last grid element, l, is

$$\begin{aligned}
&\nu_{l-\frac{1}{2}}\psi_{l-1}^{t+1} + (r_l - \nu_{l-\frac{1}{2}} - \nu_{l+\frac{1}{2}} - \omega_l)\psi_l^{t+1} \\
&= \quad -\nu_{l-\frac{1}{2}}\psi_{l-1}^{t} + (r_l + \nu_{l-\frac{1}{2}} + \nu_{l+\frac{1}{2}} + \omega_l)\psi_l^{t} - \nu_{l+\frac{1}{2}}\psi_s^{t} - \nu_{l+\frac{1}{2}}\psi_s^{t+1}, \quad (5.36)
\end{aligned}$$

where

$$r_l = \frac{4\Delta x^2 i}{\Delta t \nu_l} \tag{5.37}$$

collects prefactors for convenience and ω_l collects the potential and nonlinear terms. ψ_s^{t+1} appears on the right-hand side even though it is associated with the advanced timestep since, as a wave-generating boundary condition, it is a known value and can be incorporated there. The virtual start point and velocity of the soliton can be specified by the user. As can be seen from the simulation data in Figure 5.1, the soliton travels until it reaches the PML boundary at $x = 10$ where it gets 'stuck', begins to be absorbed and starts to spread out. The peak value of $\rho = |\psi|^2$ quickly falls to less than 0.03% of the initial value with minimal

reflectivity. The abruptness with which the PML comes into effect also has only a small effect on the reflectivity, which remains low for relatively sharp PML profiles (switching on over a distance on the order of a few Δx). Thus we can say that the PML allows us to simulate solitons propagating into empty space with good accuracy.

5.2.5 Repulsive interaction: Free expansion of a BEC

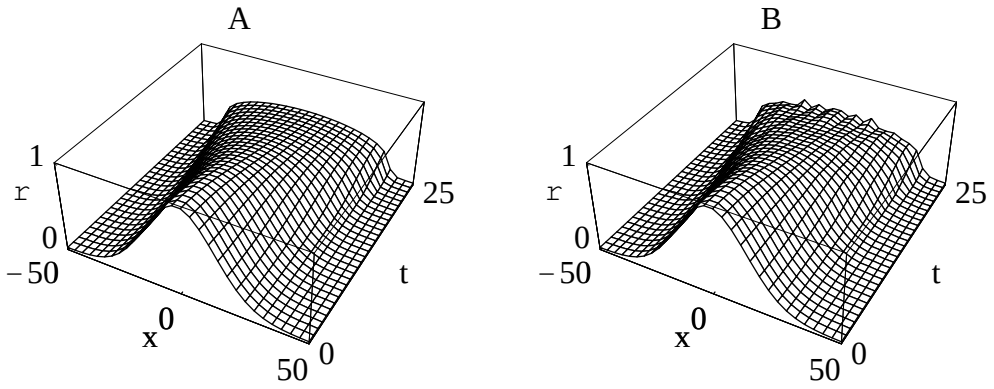

Figure 5.2: These pictures show the expansion of a condensate in a domain 100 Δx wide. In (A) the PML is placed in a $5\Delta x$-wide region on the left- and right-hand sides of the domain, while in (B) the PML is not present, which causes monotonically growing instabilities to be seen as time proceeds. The expansion with the PML is practically identical to the expansion in a $1000\Delta x$-wide domain, where the condensate does not touch the sides of the computational domain.

In a domain 100 discretization lengths in size, a condensate is prepared through the use of a Thomas-Fermi approximation [59] to obtain an initial guess for the condensate, which is then propagated in negative imaginary time to find the lowest energy state:

$$\frac{\psi_x^{t+1} - \psi_x^t}{-\Delta t_i} = \left(-(\psi_{x-1}^t - 2\psi_x^t + \psi_{x+1}^t)/\Delta x^2 + (V_x + |\psi_x^t|^2)\psi_x^t\right) \tag{5.38}$$

where Δt_i is the imaginary timestep, typically much smaller than the normal

timestep used in the simulation, and V is the trap potential used to initially confine the condensate. The condensate is then renormalized at every step by the operation

$$\psi_x^t = \psi_x^{t+1}\sqrt{N/T} \tag{5.39}$$

where N is the initial value of $\sum |\psi(x)|^2 \Delta x$ and T is the sum at the new timestep, $\sum |\psi^{t+1}(x)|^2 \Delta x$. The trap is then switched off and the condensate allowed to expand freely. The simulation results show no instabilities, even with a relatively small PML (on the order of $5\Delta x$ on the left- and right-hand sides). Without the PML, monotonically growing instabilities occur in the expanding condensate and threaten the stability of the program. When I compared the expansion with the PML in place to expansion in a computational domain 1000 discretization lengths wide, large enough that the expanding condensate does not touch its sides, no appreciable difference was evident. This indicates that the PML is functioning correctly.

Now let us turn to a system whose numerical simulation is greatly aided by the use of the Perfectly Matched Layer, the optical analogue of a Laval nozzle.

Chapter 6

One-dimensional supersonic flow of a quantum gas

As we have discussed in previous chapters, Bose-Einstein condensates should prove useful in the investigation of quantum effects of sonic horizons[1] [61]. The most basic method of creating a sonic black hole is a condensate flowing in a waveguide. This could be realized experimentally through the use of current-carrying wires in magnetic fields [62] or light beams [63] to confine the condensate. Let us consider a setup where an optical piston pushes the condensate down the waveguide through a potential barrier that plays the role of a supersonic nozzle, see Fig. 6.1. Analogous to the previous example (Section 3.3) where the sonic horizon occurred at the narrowest point of the nozzle, the sonic horizon occurs at the region where the barrier is highest. Both the piston and the barrier can be created by focussing blue-detuned light beams, which act as repulsive potentials on the condensate. The Hawking effect should then generate an extra thermal cloud of atoms near the horizon, where the effective temperature of the cloud depends on the applied confining potential. It should be feasible to distinguish this Hawking cloud from the condensate's residual thermal cloud thanks to the near-absolute zero conditions

[1] Material from this chapter originally appeared in Phys. Rev. A [60].

possible in modern condensates [33] and their dependence on the potential.

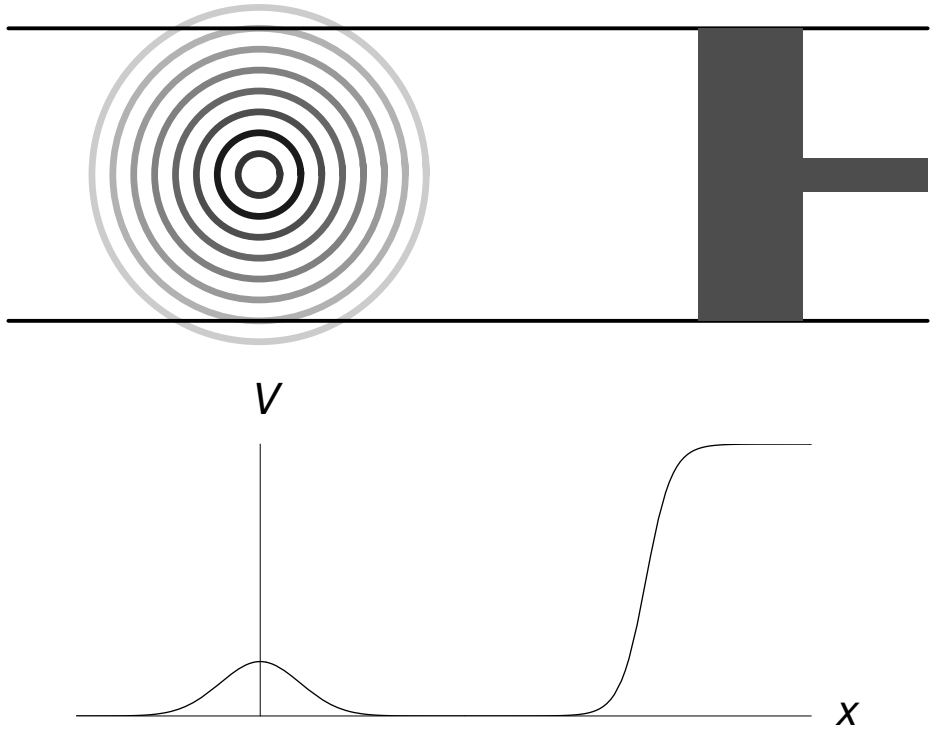

Figure 6.1: Scheme of the black hole analogue. An optical piston pushes a Bose-Einstein condensate, confined to a waveguide, over a potential barrier. Both the piston and the barrier can be created using blue-detuned light beams, which act as the potentials indicated in the lower part of the figure.

Let us calculate the required height of the potential barrier and the Hawking temperature of the sonic horizon.

6.1 One-dimensional gas flow

The theoretical model which describes the system is based on the concept of one-dimensional gas flow [64]. Two forces act on the quantum gas: the waveguide, which confines the condensate to an effective area A and the external potential U, which acts as a longitudinal force. We assume that A varies slowly and is still wide enough to treat the condensate as a 3D quantum fluid in the hydrodynamic approximation [59].

We describe the one-dimensional gas flow with particle density ρ and velocity v through area A with constant discharge Q by the equation of continuity [64]

$$\rho v A = Q\,, \tag{6.1}$$

where the velocity and density are averaged over A. The stationary gas flow obeys the Bernoulli equation [64]

$$\frac{v^2}{2} + w = \frac{\mu - U}{m}\,, \tag{6.2}$$

where μ is the chemical potential, which measures the total energy of the gas. The enthalpy w we assume to be described by the equation of state

$$w = G\rho^{\alpha}\,,\ G,\ \alpha > 0. \tag{6.3}$$

This equation of state describes a general class of gases, including Bose-Einstein condensates in the hydrodynamic approximation [59]. The constants are given by the relations

$$\alpha = 1\,,\ G = \frac{4\pi\hbar^2 a}{m^2} \tag{6.4}$$

where a is the s-wave scattering length of the condensed atoms, here a positive quantity. Equations (6.1), (6.2) and (6.3) describe how the gas adjusts to any variations in A and U which may occur along the direction of the flow.
Calculating the local speed of sound, c, according to the standard theory of sound waves in fluids [64] gives us

$$c^2 = \rho\,\frac{\partial w}{\partial \rho} = G\alpha\rho^{\alpha} = \alpha w\,. \tag{6.5}$$

Introducing the Mach number

$$\nu = \frac{v}{c} = \frac{Q}{\rho c A} = \frac{Q}{A}\,\frac{\sqrt[\alpha]{G}}{\sqrt{\alpha}}\,w^{-1/\alpha - 1/2}, \tag{6.6}$$

we can express the enthalpy w in terms of ν and also the density and local speed of sound, as

$$c = \sqrt{\alpha}\left(\frac{A}{Q}\frac{\sqrt{\alpha}}{\sqrt[\alpha]{G}}\nu\right)^{-\alpha/(2+\alpha)}, \tag{6.7}$$

$$\rho = \left(\frac{A}{Q}\sqrt{\alpha G}\,\nu\right)^{-1/(1+\alpha/2)}. \tag{6.8}$$

Any useful quantity of the one-dimensional gas flow can be expressed as a function of the Mach number within the fluid-mechanical model.

6.2 Supersonic flow

What are the conditions for the supersonic flow of a one-dimensional gas with equation of state (6.3)? Dividing the Bernoulli equation (6.2) by w, we get

$$f(\nu) = 1 \tag{6.9}$$

where

$$f = q\nu^{\alpha/(1+\alpha/2)} - \frac{\alpha}{2}\nu^2\,. \tag{6.10}$$

q is a parameter that gathers the external parameters of the system such as U and A,

$$q = \frac{\mu - U}{m}\left(\frac{A}{Q}\frac{\sqrt{\alpha}}{\sqrt[\alpha]{G}}\right)^{\alpha/(1+\alpha/2)} \tag{6.11}$$

and may depend on the longitudinal position x along the gas flow. Since the total energy μ is larger than the potential U, q is positive. The exponent $\alpha/(1+\alpha/2)$ of the first term of $f(\nu)$ in (6.10) is less than the exponent of the second term; this means that the function $f(\nu)$ has a maximum that depends on the value of q. For a critical value q_c the maximum of $f(\nu)$ occurs at $f = 1$, coinciding with the solution of the scaled Bernoulli equation. To find the maximum, differentiate

$f(\nu)$ with respect to ν:

$$\nu \frac{\partial f}{\partial \nu} = \frac{\alpha}{1+\alpha/2}\,(f-\nu^2), \tag{6.12}$$

which vanishes at $\nu = \pm 1$ for $f = 1$. Therefore when $q = q_c$, the gas flows with the local speed of sound, creating a sonic horizon. Here the function (6.10) reaches unity at

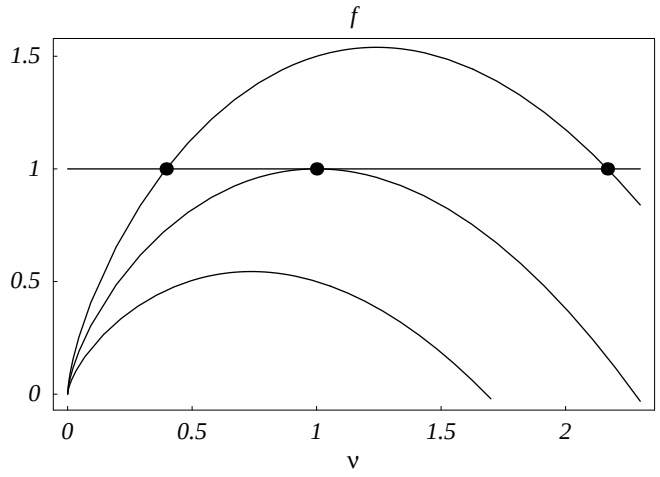

Figure 6.2: A plot of the Bernoulli function $f(\nu)$ defined in Eq. (6.10) for Bose-Einstein condensates ($\alpha = 1$). The function is plotted for three q parameters. Fluid mechanics implies that $f = 1$ for a stationary one-dimensional flow. The top curve ($q = 2$) crosses the line where $f = 1$ at two points, defining a subsonic ($\nu < 1$) and a supersonic ($\nu > 1$) regime. The central curve ($q = 3/2$) corresponds to the sonic horizon where the fluid moves with the local speed of sound ($\nu = 1$). For the lower curve ($q = 1$) no stationary flow exists.

$$q_c = 1 + \frac{\alpha}{2}\,. \tag{6.13}$$

For $q < q_c$ the curve of $f(\nu) < 1$ and therefore no stationary flow exists, while for $q > q_c$ the gas has two solutions, a subsonic and a supersonic regime; which one of the two regimes occurs depends on the evolution of the flow. An initially subsonic gas stream will stay subsonic until the flow reaches the local speed of sound. To determine how the gas behaves beyond the sonic horizon, expand q and ν in the vicinity of their critical values

$$q = q_c + \delta q\,, \quad \nu = \pm 1 + \delta\nu\,. \tag{6.14}$$

From the scaled Bernoulli equation (6.9) to lowest order in δq and $\delta\nu$, we get

$$\delta q = \frac{2\alpha}{2+\alpha}\left(\delta\nu\right)^2 . \tag{6.15}$$

Therefore, q reaches a minimum at the critical parameter, which agrees with the result that for $q < q_c$ no solution exists. Near a minimum of q, δq depends quadratically on the distance from the sonic horizon, assuming the second derivative of q does not vanish, which is generally the case, and so $\delta\nu$ is proportional to the distance. In consequence, if the flow reaches the local speed of sound the gas cannot immediately return to subsonic speed; the flow becomes supersonic. Similarly, a supersonic flow will become subsonic when q reaches q_c.

6.3 Horizons

The flow reaches the speed of sound when q is both minimal and equal to q_c. To create a stationary transsonic flow, the system parameters must be adjusted (or must adjust themselves) in accordance with the latter condition. If q at its minimum exceeds q_c, a stationary subsonic flow exists and so the gas does not become supersonic. If $q < q_c$ the piston driving the gas compresses it such that q evolves to reach q_c. The minimum of q depends on how the system parameters vary in (6.11). If the potential is constant, as in the traditional one-dimensional gas flow [64], q reaches a minimum when the area A is also minimal, *i.e.* at the waist of the nozzle. Let us suppose that the area A and potential U vary together, with

$$U = -\frac{V_0}{A^\beta} . \tag{6.16}$$

Such a relation could describe the intensity of a Gaussian light beam confining the condensate, which is inversely proportional to the area A. As the optical potential is proportional to the light intensity, $\beta = 1$. The requirement that $\partial q/\partial A$ vanishes

implies that

$$A_c = \left(\frac{\alpha\beta - 2\alpha + 2\beta}{2\alpha} \frac{V_0}{\mu} \right)^{1/\beta} . \tag{6.17}$$

In the above case of a Gaussian light beam confining a Bose-Einstein condensate,

$$A_c = \frac{V_0}{2\mu}. \tag{6.18}$$

This means that transitions from subsonic to supersonic speed and vice versa occur at a specific confining area; a Gaussian beam will establish two sonic horizons around its waist, if any.

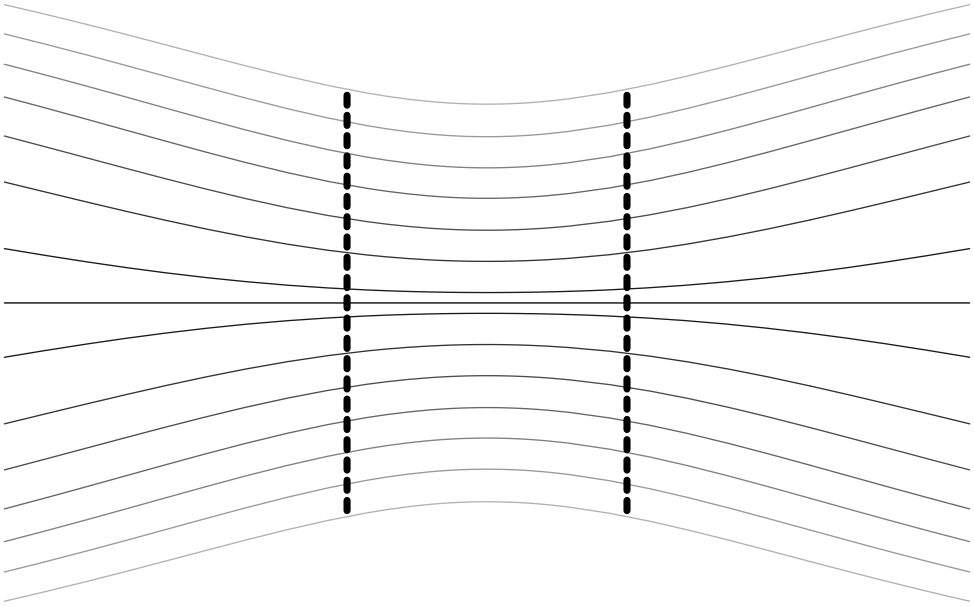

Figure 6.3: The optical analogue of the Laval nozzle, a Gaussian laser beam can both confine and focus the condensate. The interplay between longitudinal confinement and transversal forces will establish two horizons, if any: a natural double Laval nozzle.

6.4 Critical potential

When the effective confining area A stays constant along the gas flow, but U varies, the sonic horizon occurs at the potential maximum $U_{\max}$, provided that q

can adjust to q_c by changing the chemical potential μ:

$$\frac{\mu - U_m}{m} \left(\frac{A}{Q} \frac{\sqrt{\alpha}}{\sqrt[\alpha]{G}} \right)^{\alpha/(1+\alpha/2)} = 1 + \frac{\alpha}{2} \,. \tag{6.19}$$

In the setup given in Figure 6.1, for example, the driving piston compresses the gas until it reaches a stationary flow where it breaks the speed of sound at the potential maximum. The compression changes the energy of the gas, *i.e.* the chemical potential. Where the potential barrier is below the critical value U_c, supersonic flow will not occur. Let us calculate how U_c depends on the initial conditions.

Initially, the potential is zero and the gas flows with velocity v_0. Obtaining the chemical potential μ from the Bernoulli equation (6.2), we express it in terms of the initial speed of sound, c_0, and the initial (subsonic) Mach number ν_0,

$$\mu = mw_0 + \frac{m}{2} v_0^2 = \frac{mc_0^2}{\alpha} \left(1 + \frac{\alpha}{2} \nu_0^2 \right) \,. \tag{6.20}$$

The initial value of q comes from solving the scaled Bernoulli equation (6.9) for q. Expressing the solution in terms of μ we find

$$q_0 = \nu_0^{-\alpha/(1+\alpha/2)} \left(1 + \frac{\alpha}{2} \nu_0^2 \right) = \nu_0^{-\alpha/(1+\alpha/2)} \frac{\alpha \mu}{mc_0^2} \,. \tag{6.21}$$

Equation (6.11) implies that $q_c/q_0 = (\mu - U_c)/\mu$ for constant A, which gives

$$\begin{aligned} U_c &= \mu \left(1 - \frac{q_c}{q_0} \right) = \frac{mc_0^2}{\alpha} \, \eta \,, \\ \eta &= 1 + \frac{\alpha}{2} \, \nu_0^2 - \left(1 + \frac{\alpha}{2} \right) \nu_0^{\alpha/(1+\alpha/2)} \,. \end{aligned} \tag{6.22}$$

With $0 \leq \nu_0 \leq 1$ we get $1 \geq \eta \geq 0$ such that the critical potential does not exceed the initial internal energy of the gas $mw_0 = \mu - mv_0^2/2 = mc_0^2/\alpha$. $\alpha = 1$ for

Bose-Einstein condensates and so the critical potential is

$$U_c = m\left(c_0^2 + \frac{v_0^2}{2} - \frac{3}{2}\left(v_0 c_0^2\right)^{2/3}\right), \tag{6.23}$$

where v_0 is the condensate's initial flow velocity. If the applied potential barrier is less than U_c, the quantum gas will not become supersonic. Above U_c the condensate changes from subsonic to supersonic speed at the potential maximum $U_{\max}$. The driving piston compresses the quantum gas such that it always obeys (6.23) with $U_c = U_{\max}$, where in this case c_0 is the local speed of sound immediately in front of the piston and v_0 is the flow speed, *i.e.* the velocity of the piston.

6.5 Hawking temperature

As we have seen in chapter 2, the transsonic quantum gas generates the equivalent of Hawking radiation in the form of a thermal cloud of atoms. These atoms will have an effective temperature [65]

$$T = \frac{\hbar\omega_0}{2\pi k_B}\left.\frac{\partial(v \mp c)}{\partial x}\right|_{\text{horizon}}, \tag{6.24}$$

the sign being chosen as the opposite of the Mach number's at the horizon and the effective frequency ω_0 depending on the curvature of the potential, as we will see below. The Hawking temperature therefore depends on the gradient of the flow speed and the local speed of sound. Both can be expressed in terms of changes in ν. From (6.7) and the definition of the Mach number we find

$$\delta c = -\frac{\alpha c}{2+\alpha}\frac{\delta\nu}{\nu}, \quad \delta v = \nu\,\delta c + c\,\delta\nu = \frac{2c}{2+\alpha}\,\delta\nu\,. \tag{6.25}$$

In the vicinity of the maximum, the potential is approximately

$$U \approx U_m - \frac{m\omega_0^2}{2}(\delta x)^2 . \tag{6.26}$$

Expressing $\delta\nu$ in terms of δx, using (6.15) and the definition (6.11) of q for constant area,

$$(\delta\nu)^2 = \frac{2+\alpha}{2\alpha}\frac{\omega_0^2}{2}\left(\frac{A}{Q}\frac{\sqrt{\alpha}}{\sqrt[\alpha]{G}}\right)^{\alpha/(1+\alpha/2)}(\delta x)^2 , \tag{6.27}$$

The relationship (6.7) between the local speed of sound and the Mach number gives us

$$\delta v \mp \delta c = \frac{\sqrt{2+\alpha}}{2}\,\omega_0\,\delta x . \tag{6.28}$$

From this we obtain the following expression for the Hawking temperature:

$$T = \frac{\hbar\omega_0}{2\pi k_B}\frac{\sqrt{2+\alpha}}{2} . \tag{6.29}$$

For Bose-Einstein condensates where $\alpha = 1$,

$$T_{\mathrm{BEC}} = \frac{\hbar\omega_0}{2\pi k_B}\frac{\sqrt{3}}{2}, \quad m\omega_0^2 = -\left.\frac{\partial^2 U}{\partial x^2}\right|_{\mathrm{horizon}} , \tag{6.30}$$

where k_B is Boltzmann's constant. As we can see, T depends entirely on the curvature of the potential at $U_{\max}$ and on m, which together give the effective frequency ω_0, the oscillation frequency of an inverse harmonic oscillator fitted to the potential at its maximum. The factor $\sqrt{3}/2$ is the only contribution from the hydrodynamic properties of the condensate.

Creating an optical potential on the order of the condensate's mean-field energy mc_0^2 is not a serious experimental issue; the real challenge is to create a focus tight enough to generate a noticeable Hawking effect [66]. The more tightly confined the potential barrier, the larger the resulting velocity gradient at the horizon and the higher the Hawking temperature T. If the focus is of length l, the frequency ω_0

is on the order of $\sqrt{2}\,c_0/l$, if we assume that $m\omega_0^2 \approx 2U_c/l^2 \approx 2mc_0^2/l^2$. A tightly confined sodium condensate with $c_0 \approx 10^{-2}\mathrm{ms}^{-1}$, for example, has a Hawking energy k_BT of approximately 15nK if the potential is focused to $l = 10^{-6}$m. Such a thermal cloud should be measurable, given the sub-1nK condensates which can be created [33].

6.6 Numerical simulation of a 1D supersonic flow

To test the predictions of the hydrodynamic theory above, I carried out numerical simulations of the Gross-Pitaevskii equation

$$i\hbar\frac{\partial\psi}{\partial t} = -\frac{\hbar^2}{2m}\frac{\partial^2\psi}{\partial x^2} + g_A\,|\psi|^2\psi + W\psi \tag{6.31}$$

for the macroscopic wave function ψ of the condensate averaged over the longitudinal area; here g_A refers to the effective s-wave scattering coupling constant that has been averaged similarly. The potential W consists of the sum of two parts, the waveguide's confining potential

$$U = \frac{1}{2}\exp\left(-\frac{x^2}{64}\right) \tag{6.32}$$

and the optical piston potential

$$V = 5\left[1 + \frac{1}{2}\tanh(x - x_p - v_p\,t)\right], \tag{6.33}$$

where x_p is the initial position of the piston and v_p is its velocity. The piston potential is used to drive the condensate, which is initially confined between the barrier and the piston, from positive x to negative x over the potential barrier, where it reaches supersonic speed. For the simulations I used the dimensionless form of the Gross-Pitaevskii equation such that $\hbar = m = g_A = 1$, by appropriately

changing the scales of length, time and atomic density.

The initial condensate state at $t = 0$ is first determined using the Thomas-Fermi approximation [59]

$$\psi = \sqrt{0.5^2 - U(x) - V(x,0)},\ 0.5^2 - U(x) - V(x,0) > 0,$$
$$\psi = 0 \text{ otherwise,} \tag{6.34}$$

to produce an initial guess at the condensate state and then propagated in negative imaginary time in the reservoir between the potential barrier and the piston in order to find the lowest energy state for the initial potential. Finally, it is given a "kick" to match its velocity with the piston speed by multiplying it by a term $\exp[-iv_p x^2/(2x_p)]$. A perfectly-matched layer was placed at the negative x end of the computational domain to simulate the expansion of the supersonic gas into empty space. The Gross-Pitaevskii equation is solved via a Crank-Nicolson discretization

$$\begin{aligned}
&\nu_{x-\frac{1}{2}}\psi_{x-1}^{i+1} + (r_x - \nu_{x-\frac{1}{2}} - \nu_{x+\frac{1}{2}} - (2\Delta x^2/\nu_x)(U_x + V_x^i + |\psi_x^i|^2))\psi_x^{i+1} + \nu_{x+\frac{1}{2}}\psi_{x+1}^{i+1} \\
&= -\nu_{x-\frac{1}{2}}\psi_{x-1}^{i} + (r_x + \nu_{x-\frac{1}{2}} + \nu_{x+\frac{1}{2}} + (2\Delta x^2/\nu_x)(U_x + V_x^i + |\psi_x^i|^2))\psi_x^{i} \\
&- \nu_{x+\frac{1}{2}}\psi_{x+1}^{i},
\end{aligned} \tag{6.35}$$

$r_x = 4\Delta x^2 i/\Delta t \nu_x$ as before, and the use of the Thomas algorithm as described in the previous chapter. Figure 6.4 shows the density profile of the evolving condensate.

When the gas had reached a quasi-stationary regime, I compared the density profile with the above hydrodynamic theory for stationary flow. According to this theory, the profile of the Mach number, satisfying the relations (6.9) and (6.10), depends on the shape of the potential and on two additional parameters, the chemical potential μ and the ratio of the area A and the discharge Q. Equation (6.19)

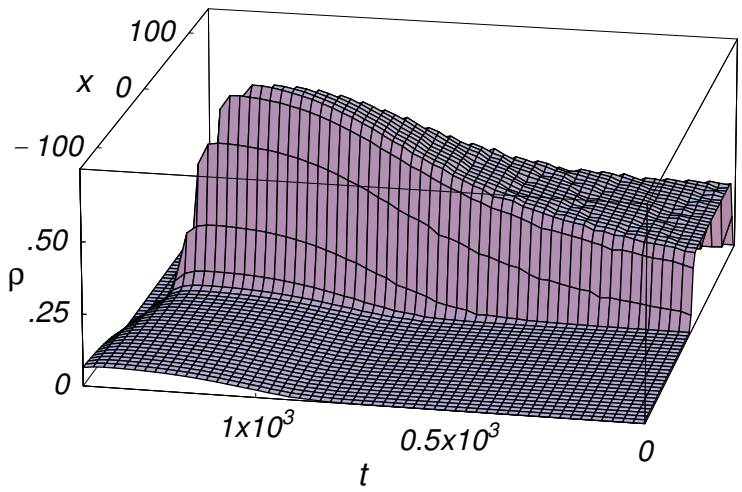

Figure 6.4: The density profile of the evolving condensate given by the numerical simulation. The optical piston compresses the condensate and pushes it over the potential barrier, as indicated in Fig. 6.1. Here the condensate becomes supersonic and its density drops dramatically. The process continues until the reservoir between piston and barrier runs out of atoms. The numerical simulations indicate that the one-dimensional transsonic flow is stable, *i.e.* one-dimensional sonic black holes should be observable without being obscured by instabilities.

connects the parameters and relates them to the maximum of the potential barrier. Effectively, only one independent parameter remains, for example the chemical potential μ. This parameter can be determined by fitting the density profile of the hydrodynamic theory, (6.8), to the numerical simulations with $\rho = |\psi|^2$ in the quasi-stationary regime. I found excellent agreement between the simulation data and the theoretical predictions, see Fig. 6.5. I also observed the 1D supersonic flow to be stable, in agreement with an earlier theoretical prediction [67].

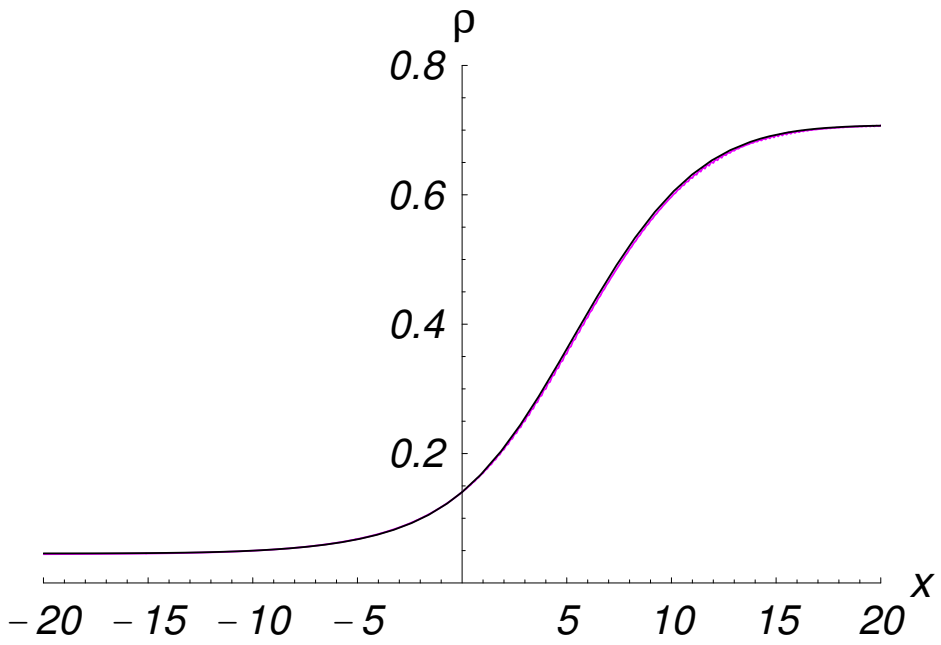

Figure 6.5: Fit of the theoretical predictions to the data from numerical simulations. The figure shows the density profile around the sonic horizon at $x = 0$. The theoretical curve (solid line) is nearly indistinguishable from the numerical simulation data (points). In the computation I assumed a piston velocity of $v_p = 0.1$ in the dimensionless units and fitted the chemical potential μ to the density profile. A value of $\mu = 0.75$ was found to give an excellent fit.

Chapter 7

The optical analogue of the Iordanskii force

7.1 Theoretical background

As we have seen previously, Bose-Einstein condensates may act as black hole analogues for sound waves and slow light. Let us investigate a different case: a vortex in a trapped BEC, illuminated by slow light. What is the behaviour of slow light in a BEC and how does it interact with the superfluid vortex?

7.1.1 Slow light in a moving BEC

We have previously discussed the theoretical background of slow light and Electromagnetically Induced Transparency in Chapter 4. Of course, it does no good to create EIT slow light in a BEC if the condensate is destroyed thereby. The probe beam should not eject atoms from the condensate via momentum transfer provided its group velocity v_g is large compared to the atomic recoil velocity [68]; given this condition the condensate should remain relatively stable.

A uniformly moving medium would simply produce a global frequency shift in the slow light, but rotation, such as of a vortex, causes a differential Doppler effect.

Consider the Lagrangian density

$$\mathcal{L} = \frac{\hbar}{2}\left((1+\alpha)(\partial_t\phi)^2 - c^2(\nabla\phi)^2 - \alpha\omega_0^2\phi^2\right). \tag{7.1}$$

We can see this is correct as the corresponding Euler-Lagrange equation describes the probe field's motion [69, 70]. Assume that this Lagrangian density is valid in frames co-moving with the medium and transform to the rest frame. Since $(\partial_t\phi)^2 - c^2(\nabla\phi)^2$ is a Lorentz invariant, consider the Doppler effect in the $\alpha(\partial_t\phi)^2$ term, assuming the condensate flow is non-relativistic. Let $\partial_t\phi \to (\partial_t + \mathbf{u}\cdot\nabla)\phi$, where $\mathbf{u}$ is the condensate's velocity profile, and discard the term quadratic in $\mathbf{u}$. The Lagrangian of light in a moving medium is then

$$\mathcal{L}_{\text{moving}} = \mathcal{L} - \alpha\mathbf{P}\cdot\mathbf{u},\ \mathbf{P} = -\hbar(\partial_t\phi)(\nabla\phi). \tag{7.2}$$

$\mathbf{P}$ is the Poynting vector of the slow light, which describes its energy flux and couples to the BEC's flow.

Since a BEC is sensitive to optical forces, being a dilute quantum fluid, we cannot simply assume that the flow remains constant and that we can treat it as a medium with set dielectric properties. We must instead consider the interplay between light and matter, considering the pair as a combined dynamical system

$$\mathcal{L}_{\text{combined}} = \mathcal{L} + \mathcal{L}_M, \tag{7.3}$$

where $\mathcal{L}_M$ is the Gross-Pitaevskii Lagrangian [23] given by

$$\mathcal{L}_M = -\rho\left(\hbar\dot{S} + \frac{m}{2}u^2 + \frac{\hbar^2}{2m}(\nabla\sqrt{\rho})^2 + \frac{g}{2}\rho + V\right), \tag{7.4}$$

ρ being the condensate's density profile, S its phase profile and the other terms having their normal meanings in the GPE context. As we have seen in Chapter

4, the degree to which each condensate atom interacts with the slow light is proportional to the induced atomic dipole moment. Exactly on the EIT resonance, the dipole moment vanishes; the detuning from this resonance frequency induces an optical force. In the EIT case, the dipole moment is linear in the detuning and hence the force on the atom is linearly dependent on the Doppler detuning due to atomic motion. From this, we can say that the degree to which each atom interacts is proportional to the scalar product of the atom velocity and the Poynting vector; in other words, the condensate sees the Poynting vector as a vector potential [71] just as the condensate's flow acts as a vector potential on the slow light. An interaction of vector potential type exists between the condensate's flow and its phase [69]

$$\mathbf{u} = \frac{\hbar}{m}\nabla S + \frac{\alpha_0}{m}\mathbf{P}, \tag{7.5}$$

where α_0 is a coupling constant which we can choose such that the propagation of slow light according to $\mathcal{L}_{\text{combined}}$ agrees with $\mathcal{L}_{\text{moving}}$ for slow light in a moving medium. By writing

$$\partial_t \rho + \nabla \cdot (\rho \mathbf{u}) = 0 \tag{7.6}$$

we see that $\mathbf{u}$ is indeed a flow according to the Euler-Lagrange equation with respect to S. Given the condition

$$\alpha = \alpha_0 \rho, \tag{7.7}$$

variations of $\mathcal{L}_{\text{combined}}$ and $\mathcal{L}_{\text{moving}}$ will agree with respect to $\mathbf{P}$ and so $\mathcal{L}_{\text{combined}}$ will indeed give us the correct wave equation of slow light in moving media.
The attendant Euler-Lagrange equation for slow light is

$$\left(\partial_t(1+\alpha)\partial_t - c^2\nabla^2 + \alpha\omega_0^2 + \partial_t\alpha\mathbf{u}\cdot\nabla + \nabla\cdot\alpha\mathbf{u}\partial_t\right)\phi = 0. \tag{7.8}$$

Near the EIT resonance frequency, the positive-frequency component of ϕ can be

represented as

$$\phi^{(+)} = \phi_0 e^{-i\omega_0 t} \tag{7.9}$$

and using a similar approximation as in Section 4.2 we can write

$$\left(i\frac{\lambda_r}{v_g}\left(\partial_t - \frac{v_g}{2v_g}\right) + \frac{1}{2}\right)\phi_0 = \frac{1}{2}\left(-i\lambda_r\nabla + \frac{\alpha}{c}\mathbf{u}\right)^2\phi_0 - \frac{\alpha^2 u^2}{2c^2}\phi_0 \tag{7.10}$$

where λ_r is the effective Planck constant reduced by 2π, $\lambda_r = c/\omega_0$. Following a similar procedure for the condensate dynamics, solving the equations of motion resulting from the Lagrangian (7.3) leads to the equation for a condensate coupled to the slow light,

$$i\hbar\frac{\partial\psi}{\partial t} = \frac{1}{2m}\left(-\hbar^2\nabla^2 - i\hbar\alpha_0\nabla\cdot\mathbf{P} - i\hbar\alpha_0\mathbf{P}\cdot\nabla\right)\psi + V\psi + g|\psi|^2\psi. \tag{7.11}$$

When slow light interacts with a vortex, it also produces a phase slip, the analogue of the Aharonov-Bohm (A-B) effect [72]; this also has a general relativity counterpart in the form of the gravitational A-B effect of a rotating cosmic string [73]. Let us discuss the Aharonov-Bohm effect in more detail.

7.1.2 The Aharonov-Bohm effect

The A-B effect was first predicted by Ehrenberg and Siday in 1949 [74] but it is better known from Aharonov and Bohm's 1959 paper [75]. In the original case, a vortex of magnetic vector potential $\mathbf{A}$ is formed around a tightly-wound solenoid, although the actual magnetic field is confined to the coil. A charged particle would not experience the magnetic vortex, but a charged wave forms an interference pattern. The phase S of the wave interacts with the vector potential for a particle with mass m, charge q and velocity $\mathbf{v}$ as

$$m\mathbf{v} = \hbar\nabla S + q\mathbf{A}. \tag{7.12}$$

Although small forces may occur due to A-B scattering [76], in the semiclassical limit the momentum density of the wave $m|\psi|^2\mathbf{v}$ is not changed and so there should be no force on either the wave or the vortex.

The case of a vortex in a BEC is not completely analogous, however. A wave in a fluid, such as a sound wave [77] sees a flow $\mathbf{u}$ as an effective vector potential $\mathbf{A}$ provided the speed of the flow is much smaller than the wave's group velocity. An analogue of the A-B effect is generated by this vector potential, but for a wave in a fluid, ∇S represents the momentum, $m\mathbf{v}$ merely acting as a pseudomomentum due to the presence of a physical background medium [78]. The A-B change in the phase therefore leads to momentum transfer between wave and fluid, exerting a force on the vortex.

If we consider a superfluid such as Helium-4, its normal component consists of elementary excitations in the large-wavelength limit, while the superfluid component is a BEC. If there is no flow of the normal component, the excitations are not directed in a particular way, instead moving randomly in the fashion of gas molecules. The total effect of the interaction between each excitation and the superfluid component's vortex causes friction [79]; this, then, is the Iordanskii force [80]. Experiments [81] indicate that it plays a significant role in the mutual friction between the normal and superfluid components but controversy has attended it, with no direct experimental evidence of its nondissipative action on vortices.

However, thanks to the fine optical control possible of alkali BECs and the ability to make their thermal components extremely small [82], the ensuing frictionless vortex motion means it should be possible to observe the optical analogue of the Iordanskii force in the optical A-B effect [31] of slow light on a vortex in an alkali BEC [83], the incoming slow light acting as a single excitation of the normal component.

In addition to the Iordanskii force, another force known as the Magnus force acts on moving vortices [84]. This force results from the rotation of the vortex as

it moves. On one side of the vortex, its flow will point in the same direction as the background flow of slow light, while on the opposite side the situation is reversed. The resulting distortion of the flow produces a force at right angles to the flow direction, its magnitude depending on the superfluid density, circulation and velocity and the vortex velocity. Let us consider in more detail the combined effect of these forces on the vortex.

7.1.3 Aharonov-Bohm generated vortex motion

We will treat both the vortex and the slow light as essentially two-dimensional objects, being homogeneous in the direction of the vortex line $\mathbf{e}$. If the vortex is fixed with flow

$$\mathbf{u}_0 = \frac{h}{m}\frac{\mathbf{e}\times\mathbf{z}}{|\mathbf{z}|^2}, \tag{7.13}$$

$\mathbf{z} = (x, y)$, then from the centre of the vortex core outward the density ρ_0 increases from zero to the bulk density ρ_B [24]. Treating the slow light which will interact with it as monochromatic, with frequency ω_0 in the laboratory frame, we can describe its positive-frequency component $\phi^{(+)}$ as resembling a plane wave with a phase slip [72]:

$$\phi^{(+)} = \sqrt{\frac{\epsilon_0}{2\hbar}}\frac{E_0}{\omega_0}\exp\left(i\mathbf{k}\cdot\mathbf{z} - i\nu\arg\mathbf{z} - i\omega_0 t\right). \tag{7.14}$$

ν is the Aharonov-Bohm flux quantum for the vortex [31],

$$\nu = \alpha\frac{\mathcal{W}\omega_0}{c^2}; \tag{7.15}$$

the vorticity of the vortex is $2\pi\mathcal{W}$ and for a single quantum vortex, $\mathcal{W} = \hbar/m$. The slower the slow light, the greater the effect on the vortex, although it must be at least two orders of magnitude greater than the bulk flow speed to avoid detuning out of the EIT frequency range (see Section 4.1). From experimental

evidence [30, 37] the maximum value of the flux quantum can be $\sim 10^{-1}$.

Consider the case where a vortex with core position $\mathbf{z}_0$ is moving at a velocity $\mathbf{v} = \mathrm{d}\mathbf{z}_0/\mathrm{d}t$ which is much less than the speed of sound. This is assumed to allow the vortex to adjust itself as it moves and remain coherent, retaining the same density and flow profiles albeit with a different centre point

$$\rho = \rho_0(\mathbf{z} - \mathbf{z}_0), \tag{7.16}$$

$$\mathbf{u} = \mathbf{u}_0(\mathbf{z} - \mathbf{z}_0) \ \text{outside the core.} \tag{7.17}$$

The slow light also follows the vortex core,

$$\phi_0^{(+)} = \phi_0^{(+)}(\mathbf{z} - \mathbf{z}_0). \tag{7.18}$$

In order to satisfy the continuity equation (7.6) when ρ varies, the condensate must constantly refill the vortex core,

$$\partial_t \rho + \nabla \cdot (\rho \mathbf{u}) = 0 = (\mathbf{u} - \mathbf{v}) \cdot \nabla \rho + \rho \nabla \cdot \mathbf{u} = (\mathbf{u} - \mathbf{v}) \cdot \nabla \rho \tag{7.19}$$

which means that $\mathbf{u} \to \mathbf{u}_0(\mathbf{z} - \mathbf{z}_0) + \mathbf{v}$ at the core. To account for this in the Gross-Pitaevskii Lagrangian (7.4), we split the kinetic energy term $\rho m u^2/2$ into $\rho_B m u^2/2$, which describes the bulk of the condensate and $(\rho - \rho_B) m (\mathbf{u} + \mathbf{v})^2/2$, which describes the back flow at the vortex core. This leads to the following variational ansatz, which reduces the motion of the vortex core to that of a point particle:

$$\begin{aligned} \mathcal{L}_M = \ & \rho \hbar \mathbf{v} \cdot \nabla S - \frac{m}{2}(\rho_0 - \rho_B)(\mathbf{u} + \mathbf{v})^2 \\ & - \frac{m}{2}\rho_B u_0^2 - \rho \left(\frac{\hbar^2}{2m} (\nabla \sqrt{\rho})^2 + \frac{g}{2}\rho + V \right), \end{aligned} \tag{7.20}$$

S being the phase profile of the vortex as given by the Aharonov-Bohm type

interaction (7.5). We minimize the action $\int L dt$ with the Lagrangian

$$L = \int\int \mathcal{L}\,\mathrm{d}x\,\mathrm{d}y = \frac{m_v}{2}v^2 + \mathbf{v}\cdot\mathbf{A}_v - U, \tag{7.21}$$

where

$$\begin{aligned} m_v &= m\int\int(\rho-\rho_B)\,\mathrm{d}x\,\mathrm{d}y, \\ \mathbf{A}_v &= \int\int(m\rho_B\mathbf{u}-\alpha\mathbf{P})\,\mathrm{d}x\,\mathrm{d}y, \\ U &= U_0 - \hbar c^2\int\int|\nabla\phi^{(+)}|^2\,\mathrm{d}x\,\mathrm{d}y. \end{aligned} \tag{7.22}$$

$\mathbf{A}_v$ and U are effective vector and scalar potentials in which the vortex moves; in the latter U_0 deals with all the Lagrangian terms barring the kinetic energy of the slow light, $\hbar c^2(\nabla\phi)^2/2$, which is averaged over the rapid oscillations of the light wave. m_v, the vortex mass, agrees with previously calculated values which take the vortex mass as exceeding the core mass due to the compressibility of condensates [85] and accounts for the negative missing mass of the vortex core.

We can see that, given these assumptions, there is a clear analogy between the case of a magnetic vortex interacting with a matter wave as in Aharonov and Bohm's original example and the light wave interacting with a matter vortex here. Calculating with respect to the vortex core position $\mathbf{z}_0$, and noting that only the long-range vortex terms depend on $\mathbf{z}_0$, we obtain the effective magnetic-like field

$$\begin{aligned} \nabla_0\times\mathbf{A}_v &= -\int\int\nabla\times(m\rho_B\mathbf{u}-\alpha\mathbf{P})\,\mathrm{d}x\,\mathrm{d}y \\ &= -\hbar\mathbf{e}(\rho_B+\nu\rho_D)\oint\frac{\mathbf{e}\times(\mathbf{z}-\mathbf{z}_0)}{|\mathbf{z}-\mathbf{z}_0|^2}\cdot\mathrm{d}\mathbf{z} \\ &= -h\mathbf{e}(\rho_B+\nu\rho_D) \end{aligned} \tag{7.23}$$

where ρ_D is the density of atomic dipoles induced by the slow light [70],

$$\rho_D = \alpha \frac{\epsilon_0 |E_p|^2}{\hbar \omega_0} = \frac{1}{2} \left| \frac{\Omega_p}{\Omega_c} \right| \rho \tag{7.24}$$

and the effective electric-like field

$$\begin{aligned} -\nabla_0 U &= \hbar \nabla \left(\mathbf{v}_g \cdot \int \int \rho_D \nu \frac{\mathbf{e} \times (\mathbf{z} - \mathbf{z}_0)}{|\mathbf{z} - \mathbf{z}_0|^2} \mathrm{d}x \mathrm{d}y \right) \\ &= \hbar \mathbf{v}_g \times \left(\nabla_0 \times \int \int \rho_D \nu \frac{\mathbf{e} \times (\mathbf{z} - \mathbf{z}_0)}{|\mathbf{z} - \mathbf{z}_0|^2} \mathrm{d}x \mathrm{d}y \right) \\ &= -\hbar \nu \rho_D \mathbf{v}_g \times \mathbf{e} \left(\oint \frac{\mathbf{e} \times (\mathbf{z} - \mathbf{z}_0)}{|\mathbf{z} - \mathbf{z}_0|^2} \cdot \mathrm{d}\mathbf{z} \right) \\ &= h \nu \rho_D \mathbf{e} \times \mathbf{v}_g, \end{aligned} \tag{7.25}$$

where $\mathbf{v}_g = v_g \mathbf{k}/(\omega_0/c)$. From this we obtain the expression

$$m_v \frac{\mathrm{d}\mathbf{v}}{\mathrm{d}t} = h\mathbf{e} \times [(\rho_B + \rho_v)\mathbf{v} + \rho_v \mathbf{v}_g], \tag{7.26}$$

where

$$\rho_v = \nu \rho_D = \frac{\epsilon_0 |E_0|^2}{m v_g^2},\ v_g \ll c, \tag{7.27}$$

which combines the Iordanskii ($h\rho_v \mathbf{e} \times \mathbf{v}_g$) and Magnus ($h\mathbf{e} \times (\rho_B + \rho_v)\mathbf{v}$) forces. Solving the dynamics [71] in the complex notation $z = x + iy$ and defining the coordinate system so that the slow light moves in the negative x direction gives

$$z_0(t) = \frac{v_D}{i\omega_c}(\exp(-i\omega_c t) - 1) + v_D t; \tag{7.28}$$

assuming the vortex can be treated like a point particle, it should drift towards the incoming slow light with velocity

$$v_D = \frac{\rho_v}{\rho_B + \rho_v} v_g \tag{7.29}$$

(neglecting ρ_v in the Magnus force term) while spiralling with the cyclotron frequency

$$\omega_c = \frac{h}{|m_v|}(\rho_B + \rho_v) = \frac{h\rho_B}{|m_v|}. \tag{7.30}$$

7.2 Numerical implementation

The optical analogue of the Iordanskii force was previously investigated by Leonhardt and Öhberg [86], but at that time they were not able to propagate the simulation for more than a short time due to contemporary hardware limitations, hence the motivation for this work.

The system to be simulated consists of the coupled pair of partial differential equations (7.10) and (7.11), which describe the dynamics of the slow light and BEC respectively. The equations are coupled via the terms

$$\mathbf{P} = -\hbar(\partial_t\phi)\nabla\phi, \tag{7.31}$$

the Poynting vector of the slow light and equation (7.5), the flow of the BEC.

The computational domain consists of a square overall domain into which the slow light enters from the positive x edge, introduced via the boundary condition in a similar fashion to the case discussed in Section 5.2.4:

$$\begin{aligned}\phi_{\text{boundary}} &= 1.28^{-10}\exp(-i\mathbf{k}x_{\max+\Delta\text{x}}) \\ &\times \frac{1}{2}\left(1+\tanh\left(\frac{1}{2}(t - x_{\max+\Delta\text{x}}/v_g)\right)\right) \\ &\times \frac{1}{2}\,\text{Re}\left[\frac{1}{\exp(\frac{i\pi}{2}(1-\tanh 0.8t))}\right].\end{aligned} \tag{7.32}$$

Here the latter two lines serve to ramp the slow light up gently over a reasonable timescale ($\sim 1-2\,\text{ms}$) to avoid any adverse effects due to suddenly perturbing the system. The domain contains a square trap which holds the condensate surrounded

by an empty region in order to minimise the influence of edge effects in the slow light calculation. Two PMLs are also used, a one-sided layer in the x-direction to catch the outgoing slow light and a two-sided layer in the y-direction to further reduce spurious finite-system-size effects (see Chapter 5).

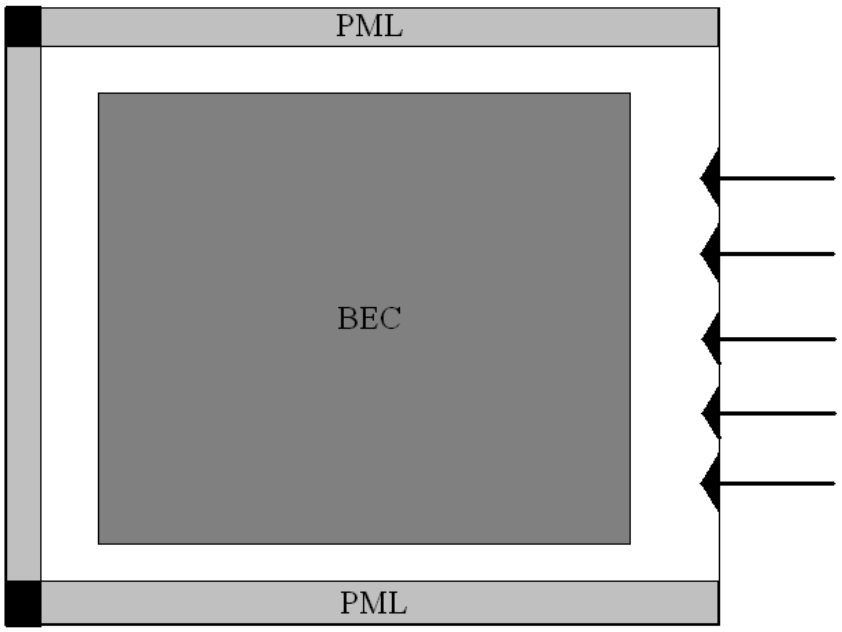

Figure 7.1: The computational domain. The BEC is confined to the centre region, with empty space around it and Perfectly Matched Layers at the edges. The slow light enters from the positive-x edge via the boundary condition (7.32).

The length and time scales used in the simulation are micrometres and milliseconds as these are the natural scales to describe the BEC-slow light system; furthermore m, the mass of a sodium atom, is set to 1 and quantities such as $\hbar$ and the scattering length are scaled accordingly. The spatial and time step sizes are $\Delta x = 0.05\mu$m and $\Delta t = 0.00025$ms. The parameters of the slow light are based on a sodium condensate; the atomic recoil velocity of sodium, v_r, is approximately $3.5 \times 10^{-2}\,\mathrm{m\,s^{-1}}$. This allows us to calculate the slow light frequency ω_0 from

$$v_r = \frac{\hbar\omega_0}{mc} \tag{7.33}$$

which gives a value for ω_0 of $3.801 \times 10^{12}\,\mathrm{ms}^{-1}$ in the scaled units.

The initial state of the condensate is prepared within the trap by negative imaginary time propagation, in a similar fashion as that described in Section 5.2.5, using the approximate Thomas-Fermi solution

$$\psi_{\text{initial}} = \sqrt{340/g} \tag{7.34}$$

inside the trap as the initial guess, where g has its usual meaning in the GPE context. The condensate trap effect is produced by defining a reduced spatial array running from grid elements (xs, ys) to (xe, ye), $xs\,, ys > x_{\text{start}}\,, y_{\text{start}}$ and $xe\,, ye < x_{\text{end}}\,, y_{\text{end}}$, and not referencing grid elements outside this area. This is equivalent to using Dirichlet boundary conditions where $\psi = 0$ outside the box and gives the effect of an infinitely high hard-wall trap beginning one grid point outside the trapped area. The vortex is also produced at this stage by imprinting the phase pattern $\sigma = (x + iy)/(x^2 + y^2)$ on the condensate at the renormalisation stage of the imaginary time propagation process,

$$\psi = \sigma|\psi_{new}|\sqrt{N/T} \tag{7.35}$$

where, as before, N is the number of atoms in the condensate and

$$T = \int |\psi_{new}(x, y)|^2 \,\mathrm{d}x\,\mathrm{d}y. \tag{7.36}$$

The highest density of this initial condensate is taken as the bulk value and used to calculate α_0 from the known value of α associated with the bulk slow light group velocity (4.27); $\alpha_0 = \alpha/|\psi_{bulk}|^2$.

Once the initial condensate is generated and the preliminary variable assignments are complete, the main Thomas algorithm loop can begin. Since there are two coupled equations, they must be advanced in parallel by calculating the coupling

terms $\mathbf{u}$ and $\mathbf{P}$ from the values of ψ and ϕ at the beginning of the loop and simultaneously updating both ψ and ϕ at the end of the loop.

Having discussed the basic parameters and methods of the simulation, let us turn to more specific details of its implementation.

7.2.1 Methodology

The nature of the slow light-BEC system makes simulating it difficult from a debugging point of view. As both equations are coupled, the source of errors, instabilities and miscellaneous other spurious behaviours can often be hard to pin down exactly. With this in mind, I treated the two components of the coupled system in so far as possible as two discrete entities; this means that both the GPE and the slow light components were first tested without the presence of the other, *i.e.* not advancing the appropriate system in time and with coupling terms set to zero, in order to find any instabilities or problems. A further advantage when debugging is the faster program runtime due to the lower number of computations involved. The slow light presented no serious problem beyond some aberrant behaviour at the $\pm y$ edges of the system, which was alleviated through use of a Perfectly Matched Layer and expansion of the slow light computational domain beyond the GPE domain such that any edge effects would be unlikely to cause errors in the condensate trap region. The use of realistic, non-scaled values in the GPE portion of the simulation, however, caused some unexpected issues.

While the slow light and Gross-Pitaevskii equations are fundamentally similar, both being modified Schrödinger equations, the addition of the nonlinear term $g|\psi|^2\psi$ in the latter complicates matters. With a strong enough nonlinearity, the standard split-step Crank-Nicholson method develops growing instabilities over time, which eventually swamp the system. Consider the simple case of a condensate at rest in a hard-wall trap. Far away from the system boundaries, the values of the condensate density will be essentially identical. As we have seen in Section

1.2, finite difference methods in situations where we perform a subtraction between two similar numbers will lead to round-off errors. The effect of the nonlinear term, however, is to magnify any differences in the computer's finite representation of the values, leading to the erroneous addition of kinetic energy. Eventually, the condensate will begin to 'bubble' with spurious excitations, rather like a kettle which boils itself. How then can we avoid this error? We could limit ourselves to very low nonlinearity [87] or a short simulation time [88], neither of which are ideal solutions as they greatly limit the class of problems we can consider. A better approach is that described by Adhikari and Muruganandam [89]: the use of a split-step method similar to the ADI method introduced in Section 5.2.2, but which separates out the nonlinear and nonderivative terms and deals with them in one step. The Gross-Pitaevskii equation with coupling terms can be written as

$$i\hbar\frac{\partial\psi}{\partial t} = \hat{H}\psi. \tag{7.37}$$

We can divide $\hat{H}$ into three parts,

$$\begin{aligned}
\hat{H}_{\mathrm{nl}} &= V + g|\psi|^2 \\
\hat{H}_x &= \frac{1}{2m}\left(-\hbar^2\nabla_x^2 - i\hbar\alpha_0\nabla_x Px - i\hbar\alpha_0 Px\nabla_x + Px^2\right) \\
\hat{H}_y &= \frac{1}{2m}\left(-\hbar^2\nabla_y^2 - i\hbar\alpha_0\nabla_y Py - i\hbar\alpha_0 Py\nabla_y + Py^2\right),
\end{aligned} \tag{7.38}$$

where Px and Py are the x- and y-components of the Poynting vector. Clearly

$$\psi^{n+1} = (\hat{H}_{\mathrm{nl}} + \hat{H}_x + \hat{H}_y)\psi^n. \tag{7.39}$$

Since there are no derivative terms in $\hat{H}_{\mathrm{nl}}$, we can apply it directly to the initial value ψ^n to produce an intermediate value $\psi^{n+1/3}$ by performing the operation

$$\psi^{n+1/3} = e^{-i\Delta t\hat{H}_{\mathrm{nl}}/\hbar}\psi_n. \tag{7.40}$$

The remaining parts of the Hamiltonian can be applied using the standard split-step Crank-Nicholson and Thomas algorithm method as described in Section 1.2.4; the discretization used is

$$\begin{aligned}
&\left(\frac{-1}{\Delta x} - \frac{1}{2i\hbar\Delta x}(Px_{x-1,y} + Px_{x,y})\right)\psi_{x-1,y}^{n+2/3} \\
&+ \left(r + \frac{2}{\Delta x} + \frac{Px_{x,y}^2}{\hbar^2}\right)\psi_{x,y}^{n+2/3} + \left(\frac{-1}{\Delta x} + \frac{1}{2i\hbar\Delta x}(Px_{x-1,y} + Px_{x,y})\right)\psi_{x+1,y}^{n+2/3} \\
&= \left(\frac{1}{\Delta x} + \frac{1}{2i\hbar\Delta x}(Px_{x-1,y} + Px_{x,y})\right)\psi_{x-1,y}^{n+1/3} + \left(r - \frac{2}{\Delta x} - \frac{Px_{x,y}^2}{\hbar^2}\right)\psi_{x,y}^{n+1/3} \\
&+ \left(\frac{1}{\Delta x} - \frac{1}{2i\hbar\Delta x}(Px_{x+1,y} + Pxx, y)\right)\psi_{x+1,y}^{n+1/3}, \qquad (7.41)
\end{aligned}$$

in the x-direction, where $r = 4m/i\hbar\Delta t$, and similarly in the y-direction for the subsequent step. As mentioned above, Dirichlet boundary conditions are used to model the hard-wall trap. The wavefunction is therefore propagated as

$$\psi^{n+1} = \hat{H}_y\hat{H}_x\hat{H}_{nl}\psi^n; \qquad (7.42)$$

splitting the discretization in this way introduces an error on the order of Δt^2, which is negligible, but greatly increases the stability for high-nonlinearity problems. The norm is, of course, conserved after each of these operations; this is confirmed by checking $\sum \psi_{x,y}\Delta x\Delta y$ at every few timesteps.

As mentioned above, the slow light, lacking nonlinearity, requires no such special measures. Equation (7.10) is discretized as

$$\begin{aligned}
&\left(\nu x_x\, \nu x_{x-\frac{1}{2},y} - \frac{1}{2\Delta x}\mu(\alpha_{x-1,y}ux_{x-1,y} + \alpha_{x,y}ux_{x,y})\right)\phi_{x-1,y} \\
&+ \left(s_{x,y} - \nu x_x(\nu x_{x-\frac{1}{2},y} + \nu x_{x+\frac{1}{2},y}) + \frac{1}{\lambda^2}\right)\phi_{x,y} \\
&+ \left(\nu x_x\, \nu x_{x+\frac{1}{2},y} + \frac{1}{2\Delta x}\mu(\alpha_{x+1,y}ux_{x+1,y} + \alpha_{x,y}ux_{x,y})\right)\phi_{x+1,y}, \qquad (7.43)
\end{aligned}$$

for the RHS of the x-step and similarly for y, where νx denotes the x-PML,

$\lambda = c/\omega_0$, $\mu = i/\lambda c$ and $s_{x,y} = 4/\Delta t v_g i\lambda$; again the standard Thomas algorithm method is used to obtain the updated slow light value. The term v_g in $s_{x,y}$ refers to the bulk group velocity, as taking the actual group velocity at each grid element proved to introduce instabilities, most likely due to the disparity between the group velocity at the vortex core, where the density is close to zero, and the group velocity in the bulk. The $\dot{\alpha}$ term in equation (7.10) is neglected as α is assumed to vary slowly.

If one wishes greater simulation accuracy (at the cost of higher computation time and memory storage requirements), one can also discretize the GPE and slow light equations using a fourth-order accurate method. However, in this case the tridiagonal Thomas algorithm no longer applies and must be extended to its pentadiagonal form. The system of equations can be represented as:

$$\begin{aligned}
c_1 u_1 + d_1 u_2 + e_1 u_3 &= f_1 \\
b_2 u_1 + c_2 u_2 + d_2 u_3 + e_2 u_4 &= f_2 \\
a_i u_{i-2} + b_i u_{i-1} + c_i u_i + d_i u_{i+1} + e_i u_{i+2} &= f_i,\ i = 3, 4 \ldots n-2. \\
a_{n-1} u_{n-3} + b_{n-1} u_{n-2} + c_{n-1} u_{n-1} + d_{n-1} u_n &= f_{n-1}. \\
a_n u_{n-2} + b_n u_{n-1} + c_n u_n &= f_n.
\end{aligned} \tag{7.44}$$

Then, letting

$$\begin{aligned}
b_2' &= b_2 \\
c_1',\ c_2' &= c_1,\ c_2 \\
d_1',\ d_2' &= d_1,\ d_2;\ d_n' = 0 \\
e_i' &= e_i,\ i < n-1;\ e_{n-1}',\ e_n' = 0 \\
f_1',\ f_2' &= f_1,\ f_2
\end{aligned} \tag{7.45}$$

set

$$\begin{aligned}
\tau &= a_i/b'_i \\
b'_{i+1} &= b_{i+1} - \tau c'_i \\
c'_{i+1} &= c_{i+1} - \tau d'_i \\
d'_{i+1} &= d_{i+1} - \tau e'_i \\
f'_{i+1} &= f_{i+1} - \tau f'_i \qquad (7.46) \\
&. \qquad (7.47)
\end{aligned}$$

Continuing, let

$$\begin{aligned}
d''_1 &= d'_1/c'_1 \\
e''_1 &= e'_1/c'_1 \\
f''_1 &= f'_1/c'_1 \qquad (7.48)
\end{aligned}$$

and

$$\begin{aligned}
\sigma_i &= 1/(c'_{i+1} - b'_{i+1}d''_i) \\
d''_{i+1} &= \sigma_i(d'_{i+1} - b'_{i+1}e''_i) \\
e''_{i+1} &= \sigma_i e'_{i+1} \\
f''_{i+1} &= \sigma_i(f'_{i+1} - b'_{i+1}f''2_i). \qquad (7.49)
\end{aligned}$$

Finally, we obtain the updated u' by the procedure

$$\begin{aligned}
u'_n &= f''_n \\
u'_{n-1} &= f''_{n-1} - d''_{n-1}u'_n \\
u'_i &= f''_i - d''_i u'_{i+1} - e''_i u'_{i+2},\ i = n-2, n-3 \ldots 1. \qquad (7.50)
\end{aligned}$$

While this formulation does provide greater accuracy, it is clear that it also requires many more operations than the tridiagonal Thomas algorithm. After experimentation, I came to the conclusion that, on the computer hardware being used, there was an insufficient return for the extra computational load and returned to the tridiagonal formulation. Use of a fourth-order accurate method could be a possible avenue for further investigation, however.

Once the individual components were judged to be stable and appeared to be working correctly, I then began to add the coupling elements. The x-component of the flow is discretized as

$$ux = \frac{-i\hbar}{2.2\Delta x}\left(\frac{\psi^*_{x,y}\left(\psi_{x+1,y}-\psi_{x-1,y}\right)-\psi_{x,y}\left(\psi^*_{x+1,y}-\psi^*_{x-1,y}\right)}{m|\psi_{x,y}|^2+\epsilon}\right), \tag{7.51}$$

and similarly for uy. This is a second-order accurate discretization; ϵ here is a small number ($\sim 10^{-4}$) which avoids division by zero at the vortex core. The $\alpha_0\mathbf{P}$ term from equation (7.5) is omitted as it should be a small effect, but its inclusion appears to lead to undesired nonlinear instability in the slow light equation for a similar reason to that of the GPE case.

The x-component of the Poynting vector is discretized as

$$Px = -i\frac{\hbar\omega_0\alpha_0}{2.2\Delta x}\left(\phi^*_{x,y}\left(\phi_{x+1,y}-\phi_{x-1,y}\right)-\phi_{x,y}\left(\phi^*_{x+1,y}-\phi^*_{x-1,y}\right)\right), \tag{7.52}$$

folding in the term α_0 for convenience since it always appears with $\mathbf{P}$; Py is discretized similarly.

Slow light interacting with a condensate vortex profile should produce an Aharonov-Bohm phase slip downstream from the vortex as we have discussed previously. To test this aspect of the interaction, I created an initial vortex profile using the negative imaginary time method described above, but did not advance it further in time. The slow light interacted with this frozen vortex profile and produced the expected phase slip pattern; see Figure 7.2.

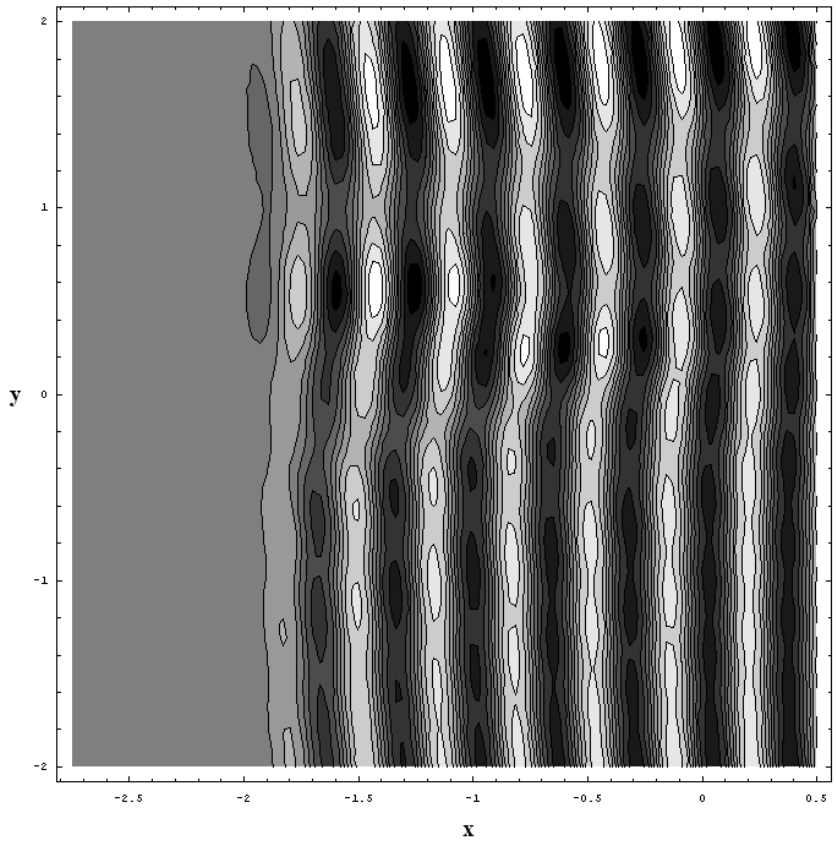

Figure 7.2: Contour plot of the real part of the slow light, showing the Aharonov-Bohm phase slip which results from interaction with the flow pattern of a vortex centred at $(0, 0)$.

Unfortunately, the condensate portion of the program has no such easy test. Under the effects of a constant Poynting vector throughout the domain, which is not a useful case in general but suffices for limited testing purposes, the vortex flow pattern undergoes a gauge transformation. Preparing a vortex, I increased the value of the Poynting vector from zero to $10^{-15}\mathbf{x} + 10^{-15}\mathbf{y}$, using a tanh ramping function similar to that used in the slow light boundary condition in order to avoid any unusual effects from shocking the system. As expected, the vortex adjusted to the slow light, deforming slightly.

Once the preliminary coupling tests were complete, I began simulating the full coupled system of equations. In general in the simulations, $N = 2.103 \times 10^3$, $v_g = 355\,\mu\mathrm{m\,ms}^{-1}$ and the computational domain was $3.5 \times 3.5\,\mu\mathrm{m}^2$, with the trap

beginning 0.25 μm in from the computational domain boundary.

7.3 Results

As we will recall from earlier in the chapter, the expected behaviour of the vortex was to move towards the incoming slow light with the velocity (7.29), while spiralling with the cyclotron frequency (7.30). This is not what I observed in my simulations, however. Instead, after initially being pushed in the negative x-direction, the magnitude of the movement depending on the steepness of the incoming slow light profile as well as its magnitude, the vortex begins to move towards the incoming slow light but instead soon settles into spiral motion around a point near the centre of the trap; this motion's centre point appears to move very slowly in the positive $x-$ and $y-$directions. After approximately 16μs the vortex motion, while displaying the same basic character, becomes more erratic; it is possible this could be due to an accumulation of error or simply a result of the physics of the coupled system. I am confident, however, that the earlier portion of the vortex motion is a genuine result of the slow light-vortex interaction.

As the vortex core's position does not strictly coincide with grid points for the vast majority of the program runtime, one can only get a crude picture of its progress by performing a minimum search for the lowest density grid point at each timestep and plotting the resulting data. To determine the position of the vortex core more accurately, I sampled a 10×10 section of the grid points around the condensate centre every 40 timesteps and used Mathematica to construct an interpolation of the data, which gives a much smoother description of the vortex core's motion; Figure 7.3 shows the position of the vortex core over 15μs.

Why, then, does the vortex not spiral towards the incoming slow light, as expected? The theory given earlier was predicated on the flow pattern around the vortex remaining constant and moving with the vortex core. Figure 7.4 shows the

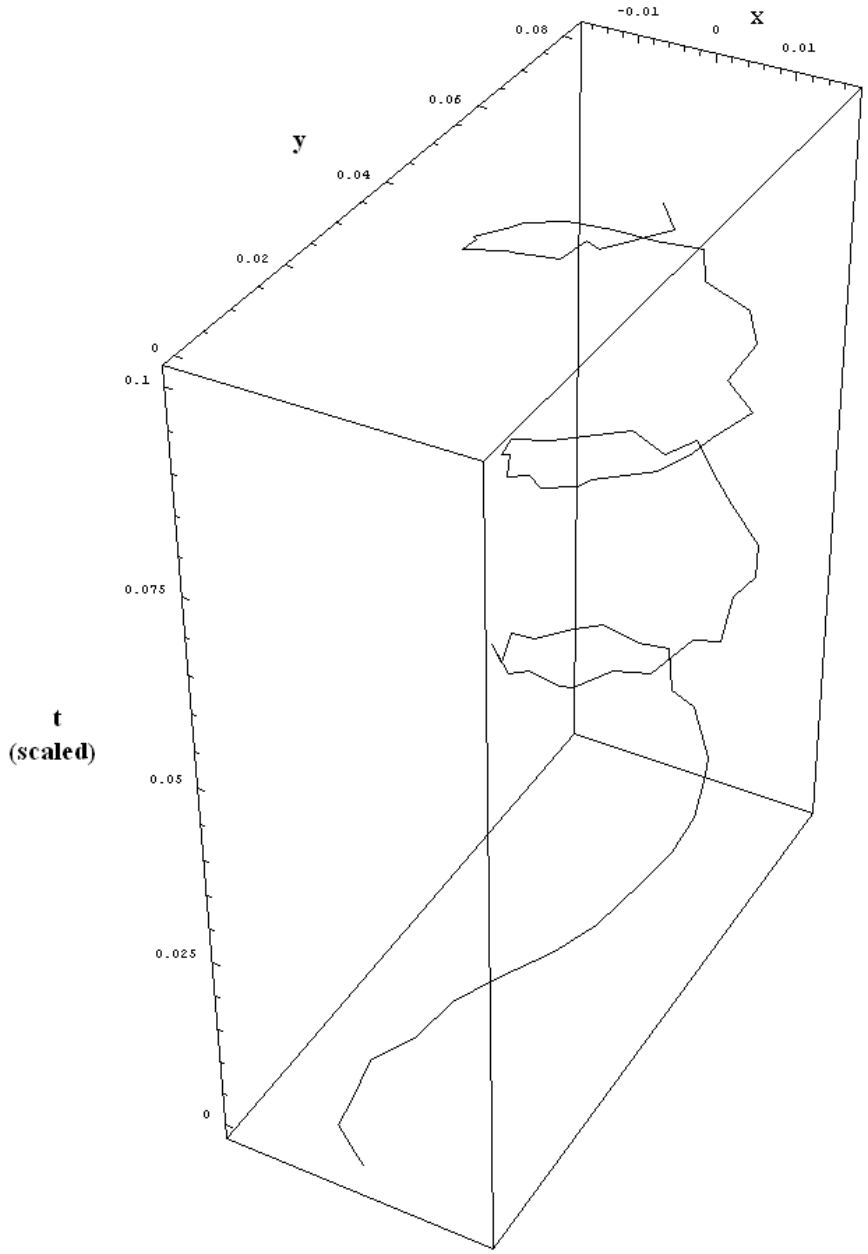

Figure 7.3: Motion of the vortex core under the effects of slow light over 15μs. The vortex is initially pushed by the slow light, then begins to move towards it, eventually spiralling around a point near the centre of the trap.

real part of the initial flow pattern around the vortex, which is regular. In this simulation, however, the flow pattern becomes distorted as it moves. Figure 7.5 shows the real part of the flow pattern after $\sim 14\mu$s of program runtime. In order to rule out the possibility that this distortion was an artefact of the condensate dynamics, I allowed a vortex to evolve for 10μs without any slow light. Dividing the Fourier transforms of the initial flow data by the Fourier transforms of the final flow data, I found the resulting terms very close to 1, as one would expect if the flow pattern were essentially the same except for minor variances. Performing the same procedure in the case where slow light was present gave results $\gg 1$, showing a large variance from the initial flow pattern. To investigate the possibility of this flow distortion being due to the finite size effect of the trap, I performed the simulation in a trap of $7 \times 7\mu$m and observed a similar behaviour of the flow pattern. The above tests lead me to conclude that this is a genuine property of the coupled system; as the simple assumption of the theory that the flow remains constant is not valid, it is not surprising that its predictions of the vortex behaviour are also not borne out. While the theory given in Section 7.1.3 could apply for very short timescales, finding a theory which takes the distortion of the vortex flow pattern into account is not a trivial task, and could be a possible avenue for further investigation.

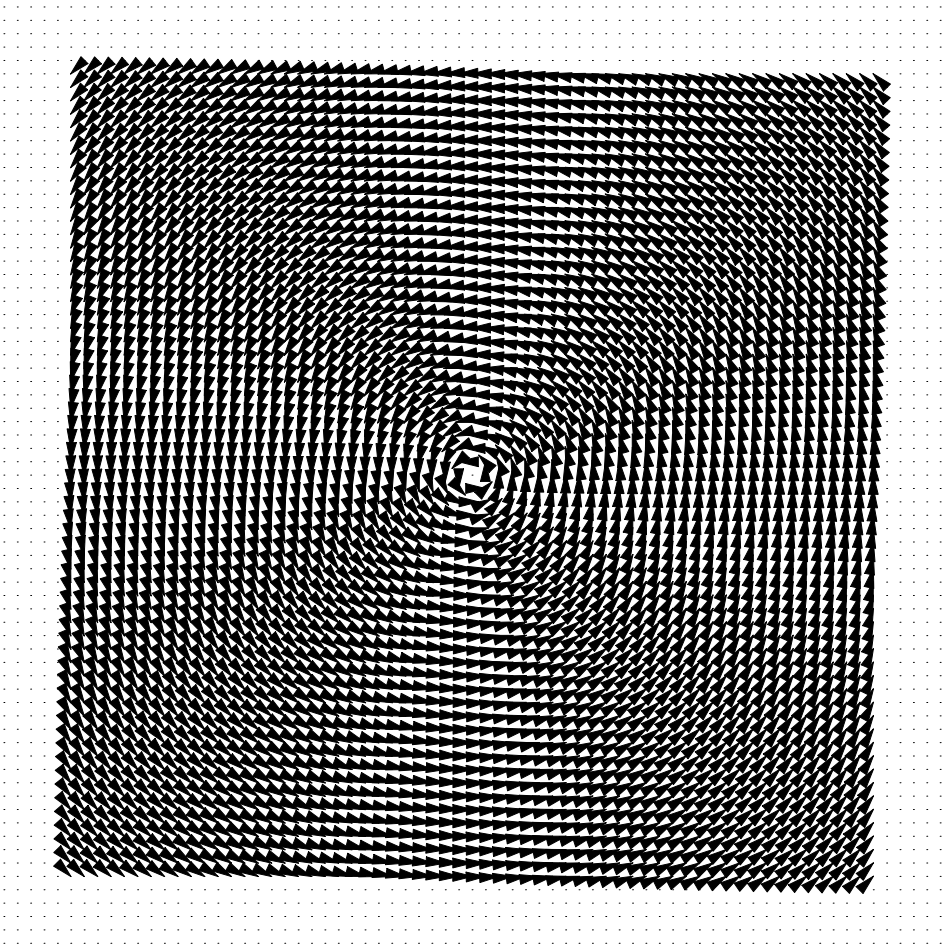

Figure 7.4: The real part of the initial flow pattern around the vortex, generated by imposing the vortex profile on the condensate during negative imaginary time propagation. Under the assumptions of the theory described earlier, this flow pattern should remain constant around the vortex as it moves under the influence of the slow light.

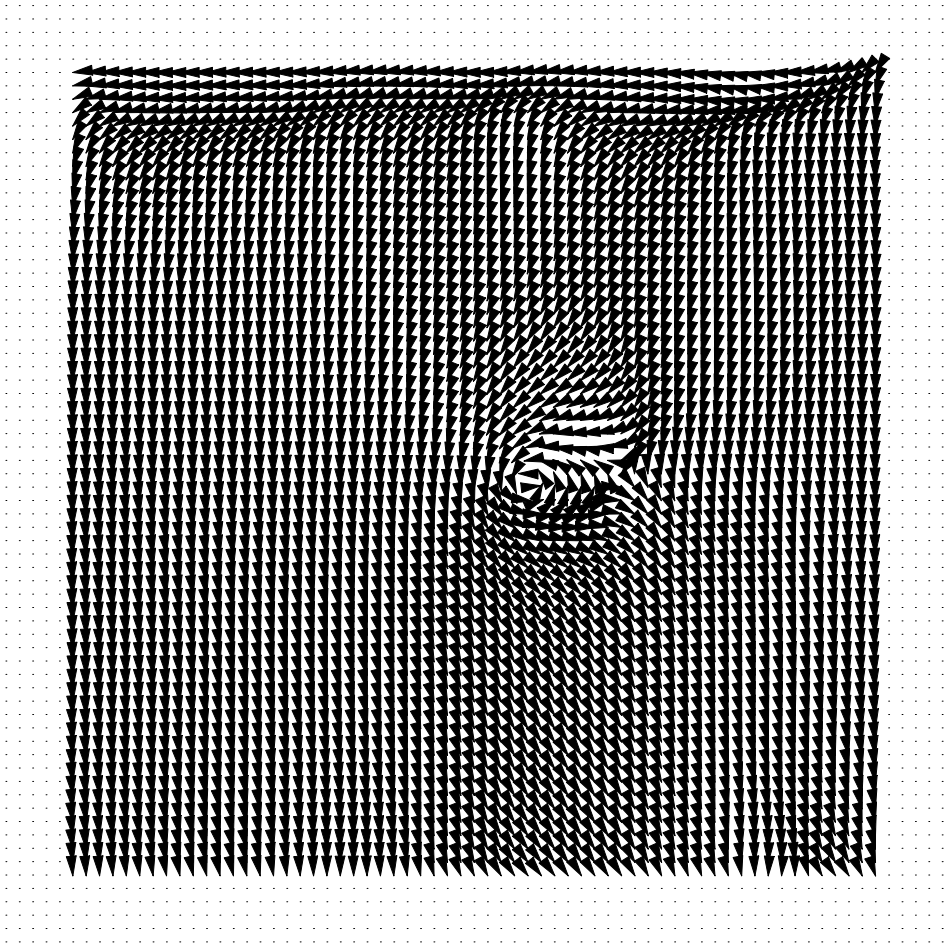

Figure 7.5: The real part of the flow pattern around the vortex after $\sim 14\mu$s of interaction with the slow light. We can see that the expectation that the flow should remain constant is not borne out and instead the flow has been distorted.

Conclusions

In this thesis, we have explored the links between different ways of modelling reality. In Chapter 1, we discussed how to render physical problems in numerical form. We have seen that while this technique has its limitations, it is a useful and robust way of investigating physical systems and even predicting their behaviour. In Chapter 2, we turned to a different way of modelling reality, probing gravitational black holes through the use of analogue models such as supersonic flow of a Bose-Einstein condensate. Many important elements of the physics of these astronomical objects are mirrored in their analogues. Chapter 3 further investigated BECs, the new form of matter which results from bosons occupying the same energy state at fantastically low temperatures. After investigating the mean-field equation which describes BEC dynamics, the Gross-Pitaevskii equation, we moved on to another element useful in black hole analogues, slow light. Chapter 4 dealt with one of the techniques by which light's group velocity may be slowed to the order of metres per second, Electromagnetically Induced Transparency. Chapter 5 discussed the application of the Perfectly Matched Layer absorbing boundary condition to nonlinear and matter wave systems. As my numerical simulations show, the Perfectly Matched Layer can be used to good effect in simulations of such systems by truncating the domain, which not only increases computational efficiency but also increases stability. In Chapter 6 we began to tie all the disparate strands together as we discussed the numerical simulation of a black hole analogue, the supersonic flow of a BEC in a Laval nozzle. The simulation is greatly assisted by

the PML and its results also agree well with the hydrodynamic theory of the flow, which indicates that it is accurate. From the simulation we can predict that such a supersonic flow should be stable and may be observable in a laboratory. Chapter 7 discussed another simulation, the optical analogue of the Iordanskii force, which is investigated by illuminating a vortex with slow light. This simulation, however, is greatly more intricate than the previous chapter's, involving two coupled partial differential equations in 2+1 dimensions. The results of the simulation showed that the simple theory used to describe the vortex behaviour did not apply, as the vortex's flow pattern was distorted instead of remaining fixed.

Bibliography

[1] Euler L, 1768, *Institutiones Calculi Integralis* (St. Petersburg).

[2] Richardson L F, 1925, *Mathl. Gaz.*, **12**, 415.

[3] Landau E, 1927, *Vorlesungen über Zahlentheorie*, Vol. 2 (Leipzig).

[4] Unruh W, 1981, *Experimental Black-Hole Evaporation?*, Phys. Rev. Lett. **46**, 1351.

[5] Hawking S W, 1974, *Black Hole Explosions?*, Nature (London) **248**, 30.

[6] Hawking S W, 1975, *Particle creation by black holes*, Commun. Math. Phys. **43**, 199.

[7] Visser M, 1998, *Hawking Radiation without Black Hole Entropy*, Phys. Rev. Lett. **80**, 3436.

[8] Leonhardt U, Kiss T and Ohberg P, 2003, *Bogoliubov theory of the Hawking effect in Bose-Einstein condensates* , J. Opt. B **5**, S42.

[9] Barceló C, Liberati S, Sonego S and Visser M, 2006, *Hawking-Like Radiation Does Not Require a Trapped Region*, Phys. Rev. Lett. **97**, 171301.

[10] Volovik G E, *Black-hole horizon and metric singularity at the brane separating two sliding superfluids*, JETP Lett. **76**, 240 (2002).

[11] Jacobson T, 1999, *Trans-Planckian redshifts and the substance of the space-time river*, Prog. Theor. Phys. Suppl. **136**, 1.

[12] Volovik G E, 2003, *The Universe in a Helium Droplet*, (Oxford: Clarendon).

[13] Tilley D R and Tilley J, 1996, *Superfluidity and Superconductivity*, (Bristol: IOP).

[14] Birrell N D and Davies P C, 1982, *Quantum Fields In Curved Space*, (Cambridge: Cambridge University Press).

[15] Bose S, 1924, *Plancks Gesetz und Lichtquantenhypothese*, Zeitschrift für Physik **26**, 178.

[16] Einstein A, 1924, *Quantentheorie des einatomigen idealen gases*, Sitzungsberischte der Preussische Akademie der Wissenschaften, Berlin, 261.

[17] Anderson M H, Ensher J R, Matthews M R, Wieman C E and Cornell E A, 1995, *Observation of Bose-Einstein Condensation in a Dilute Atomic Vapor*, Science **269**, 198.

[18] Davis K B, Mewes M-O, Andrews M R, van Druten N J, Durfee D S, Kurn D M and Ketterle W, 1995, *Bose-Einstein Condensation in a Gas of Sodium Atoms*, Phys. Rev. Lett. **75**, 3969.

[19] Regal C A, Greiner M and Jin D S, 2004, *Observation of Resonance Condensation of Fermionic Atom Pairs*, Phys. Rev. Lett. **92**, 040403.

[20] Gross E P, 1957, *Unified Theory of Interacting Bosons*, Phys. Rev. **106**, 161.

[21] Ginzburg V L and Pitaevskii L P, 1958, Sov. Phys. JETP **7**, 858.

[22] Bogoliubov N N, 1947, J. Phys (Moscow) **11**, 23.

[23] Dalfovo F, Giorgini S, Pitaevskii L P and Stringari S, 1999, *Bose-Einstein condensation in trapped gases*, Rev. Mod. Phys. **71**, 463.

[24] Fetter A L and Svidzinsky A A, 2001, *Vortices in a trapped dilute Bose-Einstein condensate*, J. Phys. Condens. Matt. **13**, R135.

[25] Lobo C, Sinatra A and Castin Y, 2004, *Vortex Lattice Formation in Bose-Einstein Condensates*, Phys. Rev. Lett. **92**, 020403.

[26] Mewes M-O, Andrews M R, Kurn D-M, Durfee D S, Townsend CG and Ketterle W, 1997, *Output Coupler for Bose-Einstein Condensed Atoms*, Phys. Rev. Lett. **78**, 582; Inouye S, Pfau T, Gupta S, Chikkatur A P, Görlitz A, Pritchard D E and Ketterle W, 1999, *Phase-coherent amplification of atomic matter waves*, Nature **402**, 641; Kozuma M, Suzuki Y, Torii Y, Sugiura T, Kuga T, Hagley E W and Deng L, 1999, *Phase-Coherent Amplification of Matter Waves*, Science **286**, 2309.

[27] Unruh W G, 1995, *Sonic analogues of black holes and the effects of high frequencies of black hole evaporation, Phys. Rev. D* **51**, 2827.

[28] Novello M, Visser M and Volovik G E (eds.), 2002, *Artificial Black Holes* (Singapore: World Scientific).

[29] Novello M, Visser M and Volovik G E (eds.), 2002, *Artificial Black Holes*, Chapter 2 (Singapore: World Scientific).

[30] Hau L V, Harris S E, Dutton Z and Behroozi C H, 1999, *Light speed reduction to 17 metres per second in an ultracold atomic gas*, Nature (London) **397**, 594.

[31] Leonhardt U and Piwnicki P, 2000, *Relativistic Effects of Light in Moving Media with Extremely Low Group Velocity*, Phys. Rev. Lett. **84**, 822.

[32] Scully M O and Zubairy M S, 1997, *Quantum Optics* (Cambridge: Cambridge University Press).

[33] Leanhardt A E, Pasquini T A, Saba M, Schirotzek A, Shin Y, Kielpinski D, Pritchard D E and Ketterle W, 2003, *Cooling Bose-Einstein Condensates Below 500 Picokelvin*, Science **301**, 1513.

[34] Jackson J D, 1975, *Classical Electrodynamics* (New York: Wiley).

[35] Lindblad G, 1976, *On the generators of quantum dynamical semigroups*, Commun. Math. Phys. **48**, 119.

[36] Gardiner C W, 1991, *Quantum Noise* (Berlin: Springer).

[37] Liu C, Dutton Z, Behroozi C H and Hau L V, 2001, *Observation of coherent optical information storage in an atomic medium using halted light pulses*, Nature (London) **409**, 490.

[38] Philips D F, Fleischhauer A, Mair A, Walsworth R L and Lukin M D, 2001, *Storage of Light in Atomic Vapor*, Phys. Rev. Lett. **86**, 783.

[39] Fleischhauer M and Lukin M D, 2000, *Dark-State Polaritons in Electromagnetically Induced Transparency*, Phys. Rev. Lett. **84**, 5094.

[40] , Farrell C and Leonhardt U, 2005, *The Perfectly Matched Layer for nonlinear and matter waves*, J. Opt. B, **7**, 1-4.

[41] Berenger J-P, 1994, *A Perfectly Matched Layer For The Absorption Of Electromagnetic Waves*, Journal of Computational Physics **114**, 185

[42] Andrew W V, Balanis C A and Tirkas P A, June 1995, *A Comparison Of The Berenger Perfectly Matched Layer And The Lindman Higher-Order ABCs For The FDTD Method*, IEEE Microwave and Guided Wave Letters **5**, 192.

[43] Mittra R and Pekel Ü, March 1995, *A new look at the perfectly matched layer (PML) concept for the reflectionless absorption of electromagnetic waves, IEEE Microwave and Guided Wave Letters* **5**, 84.

[44] Demoerloose J and Stuchly M A, October 1995, *Behaviour of Berenger ABC for evanescent waves, IEEE Microwave and Guided Wave Letters* **5(10)**, 344.

[45] Wu Z and Fang J, 1995, *Numerical Implementation and Performance of Perfectly Matched Layer Boundary Condition for Waveguide Structures, IEEE Transactions on Microwave Theory and Techniques* **43**, 2676.

[46] Veihl J C and Mittra R, 1996, *An efficient implementation of Berenger's perfectly matched layer (PML) for finite-difference time-domain mesh truncation, IEEE Microwave and Guided Wave Letters* **6**, 94.

[47] Xu J, Ma J G and Chen Z Z, 1998 *Numerical validations of a nonlinear PML scheme for absorption of nonlinear electromagnetic waves, IEEE Trans. Microw. Theory Tech.* **46**, 1752.

[48] Hastings F D, Schneider J B and Broschat S L, 1996 *Application of the perfectly matched layer (PML) absorbing boundary condition to elastic wave propagation, Journal of the Acoustical Society of America* **100**, 3061.

[49] Liu Q H and Tao J P, 1997 *The perfectly matched layer for acoustic waves in absorptive media, Journal of the Acoustical Society of America* **102**, 2072.

[50] Zeng Y Q and Liu Q H, 2001, *A staggered-grid finite-difference method with perfectly matched layers for poroelastic wave equations, J. Acoust. Soc. Am.* **109**, 2571.

[51] Zeng Y Q, He J Q and Liu Q H, 2001, *The application of the perfectly matched layer in numerical modeling of wave propagation in poroelastic media, Geophysics* **66**, 1258.

[52] Oguz U and Gurel L, 2002, *Frequency responses of ground-penetrating radars operating over highly lossy grounds, IEEE Trans. Geosci. Remote Sens.* **40**, 1385.

[53] Deschamps G A, 1971, *Gaussian beams as a bundle of complex rays, Electron. Lett.* **7**, 684.

[54] Chew W C and Weedon W, 1994, *A 3D perfectly matched medium from modified Maxwell's equations wth stretched coordinates, Microw. Opt. Technol. Lett.* **7**, 599.

[55] Agrawal G P, 1995, *Nonlinear Fiber Optics* (San Diego: Academic Press).

[56] Strecker K E, Partridge G B, Truscott A G and Hulet R G, 2002, *Formation and propagation of matter-wave soliton trains, Nature* **417**, 150.

[57] Thomas L H, 1949 *Elliptic problems in linear differential equations over a network*, Watson Sci. Comp. Lab., Columbia University, New York.

[58] Douglas Jr. J, 1955, *On the Numerical Integration of* $\frac{\partial^2 u}{\partial x^2} + \frac{\partial^2 u}{\partial y^2} = \frac{\partial u}{\partial t}$ *by Implicit Methods*, J. Soc. Ind. Appl. Math. **3**, 42; Peaceman D W and Rachford H H, 1955, *The Numerical Solution of Parabolic and Elliptic Differential Equations*, J. Soc. Ind. Appl. Math. **3**, 28; Douglas Jr. J and Rachford H H, 1956, *On the Numerical Solution of Heat Conduction Problems in Two and Three Space Variables*, Trans. Am. Math. Soc. **82**, 421.

[59] Pitaevskii L P and Stringari S, 2003, *Bose Einstein Condensation*, (Oxford: Clarendon Press).

[60] Giovanazzi S, Farrell C, Kiss T and Leonhardt U, 2004, *Conditions for one-dimensional supersonic flow of quantum gases*, Phys. Rev. A **70**, 063602-1-6.

[61] Garay L J, Anglin J R, Cirac J I and Zoller P, 2000, *Sonic Analog of Gravitational Black Holes in Bose-Einstein Condensates*, Phys. Rev. Lett. **85**, 4643; Garay L J, Anglin J R, Cirac J I and Zoller P, 2001, *Sonic black holes in dilute Bose-Einstein condensates*, Phys. Rev. A **63**, 023611.

[62] Denschlag J, Cassettari D and Schmiedmayer J, 1999, *Guiding Neutral Atoms with a Wire*, Phys. Rev. Lett. **82**, 2014.

[63] Görlitz A, Vogels J M, Leanhardt A E, Raman C, Gustavson T L, Abo-Shaeer J R, Chikkatur A P, Gupta S, Inouye S, Rosenband T and Ketterle W, 2001, *Realization of Bose-Einstein Condensates in Lower Dimensions*, Phys. Rev. Lett. **87**, 130402.

[64] Landau L D and Lifshitz E M, 1982, *Fluid Mechanics*, (Oxford: Pergamon).

[65] Visser M, 1998, *Acoustic black holes: horizons, ergospheres and Hawking radiation*, Class. Quant. Grav. **15**, 1767.

[66] Shin Y, Saba M, Schirotzek A, Pasquini T A, Leanhardt A E, Pritchard D E and Ketterle W, 2004, *Distillation of Bose-Einstein Condensates in a Double-Well Potential*, Phys. Rev. Lett. **92**, 150401; Shin Y, Saba M, Pasquini T A, Ketterle W, Pritchard D E and Leanhardt A E, 2004, *Atom Interferometry with Bose-Einstein Condensates in a Double-Well Potential*, Phys. Rev. Lett. **92**, 050405.

[67] Leonhardt U, Kiss T and Öhberg P, 2003, *Theory of elementary excitations in unstable Bose-Einstein condensates and the instability of sonic horizons*, Phys. Rev. A **67**, 033602.

[68] Dutton Z, Budde M, Slowe C and Hau L V, 2001, *Observation of Quantum Shock Waves Created with Ultra- Compressed Slow Light Pulses in a Bose-Einstein Condensate*, Science **293**, 663.

[69] Landau L D and Lifshitz E M, 1977, *Quantum Mechanics*, (Oxford: Pergamon).

[70] Novello M, Visser M and Volovik G E (eds.), 2002, *Artificial Black Holes*, Chapter 3 (Singapore: World Scientific).

[71] Landau L D and Lifshitz E M, 1975, *The Classical Theory of Fields*, (Oxford: Pergamon).

[72] Leonhardt U and Piwnicki P, 2001, *Slow light in moving media*, J. Mod. Optics **48**, 977.

[73] Volovik G E, 1998, JETP Lett. **67**, 881.

[74] Ehrenberg W and Siday R E, 1949, *The Refractive Index in Electron Optics and the Principles of Dynamics*, Proc. Phys. Soc. **B62**, 8.

[75] Aharonov Y and Bohm D, 1959, *Significance of electromagnetic potentials in quantum theory*, Phys. Rev. **115**, 485.

[76] Shelankov A L, 1998, *Magnetic force exerted by the Aharonov-Bohm line*, Europhys. Lett. **43**, 623.

[77] Berry M V, Chambers R G, Large M D, Upstill C and Walmsley J C, 1980, *Wavefront dislocations in the Aharonov-Bohm effect and its water wave analogue*, Eur. J. Phys. **1**, 154.

[78] Stone M, 2000, *Phonons and Forces: Momentum versus Pseudomomentum in Moving Fluids*, cond-mat/0012316.

[79] Kopnin N B, 2002, *Vortex dynamics and mutual friction in superconductors and Fermi superfluids*, Rep. Prog. Phys. **65**, 1633.

[80] Iordanskii S V, 1964, *On the mutual friction between the normal and superfluid components in a rotating Bose gas*, Ann. Phys. **29**, 335.

[81] Barenghi C F, Donnelly R J and Vinen W F, 1983, *Friction on quantized vortices in helium II. A review*, J. Low Temp. Phys. **52**, 189.

[82] Jin D S, Matthews M R, Ensher J R, Wieman C E and Cornell E A, 1997, *Temperature-Dependent Damping and Frequency Shifts in Collective Excitations of a Dilute Bose-Einstein Condensate*, Phys. Rev. Lett. **78**, 764.

[83] Matthews M R, Anderson B P, Haljan P C, Hall D S, Wieman C E and Cornell E A, 1999, *Vortices in a Bose-Einstein Condensate*, Phys. Rev. Lett. **83**, 2498.

[84] Hall H E and Vinen W F, 1956, *The Rotation of Liquid Helium II. II. The Theory of Mutual Friction in Uniformly Rotating Helium II*, Proc. R. Soc. London, Ser. A **238**, 215.

[85] Duan J-M, 1994, *Mass of a vortex line in superfluid ^{4}He: Effects of gauge-symmetry breaking*, Phys. Rev. B **49**, 12381.

[86] Leonhardt U and Öhberg P, 2003, *Optical analog of the Iordanskii force in a Bose-Einstein condensate*, Phys. Rev. A **67**, 053616.

[87] Ruprecht P A, Holland M J and Burnett K, 1995, *Time-dependent solution of the nonlinear Schrödinger equation for Bose-condensed trapped neutral atoms*, Phys. Rev. A, **51**, 4704.

[88] Dalfovo F and Stringari S, 1996, *Bosons in anisotropic traps: Ground state and vortices*, Phys. Rev. A **53**, 2477.

[89] Adhikari S K and Muruganandam P, 2002, *Bose-Einstein condensation dynamics from the numerical solution of the Gross-Pitaevskii equation*, J. Phys. B **35**, 2831.